Identification of pharmacological inducers of a reversible hypometabolic state for whole organ preservation

Megan M. Sperry[1,2], Berenice Charrez[1], Haleh Fotowat[1], Erica Gardner[1], Kanoelani Pilobello[1], Zohreh Izadifar[1], Tiffany Lin[1], Abigail Kuelker[1], Sahith Kaki[1], Michael Lewandowski[1], Shanda Lightbown[1], Ramses Martinez[1], Susan Marquez[1], Joel Moore[1], Maria Plaza-Oliver[1,3], Adama M. Sesay[1], Kostyantyn Shcherbina[1], Katherine Sheehan[1], Takako Takeda[1], Daniela Del Campo[1], Kristina Andrijauskaite[4], Exal Cisneros[4], Riley Lopez[4], Isabella Cano[4], Zachary Maxwell[4], Israel Jessop[4], Rafael J. Veraza[4], Leon Bunegin[4], Thomas J. Percival[5], Jaclyn Yracheta[5], Jorge Pena[5], Diandra Wood[5], Zachary Homas[5], Cody Hinshaw[5], Jennifer Cox-Hinshaw[5], Olivia G. Parry[5], Justin J. Sleeter[5], Erik K. Weitzel[5], Michael Levin[1,2,6], Michael Super[1], Richard Novak[1], Donald E. Ingber[1,7,8]*

[1]Wyss Institute for Biologically Inspired Engineering at Harvard University
[2]Department of Biology, Tufts University,
[3]DEVANA group, Faculty of Pharmacy, University of Castilla-La Mancha
[4]Vascular Perfusion Solutions, Inc
[5]RESTOR™, 59th Medical Wing, JBSA, Lackland AFB
[6]Allen Center, Tufts University
[7]Vascular Biology Program & Department of Surgery, Boston Children's Hospital and Harvard Medical School
[8]Harvard John A. Paulson School of Engineering and Applied Sciences
*Corresponding author: Donald E. Ingber, MD, PhD, Wyss Institute at Harvard University, 201 Brookline Ave., Suite 401, Boston, MA, 02215 USA (Em: don.ingber@wyss.harvard.edu)

ABSTRACT

Drugs that induce reversible slowing of metabolic and physiological processes would have great value for organ preservation, especially for organs with high susceptibility to hypoxia-reperfusion injury, such as the heart. Using whole-organism screening of metabolism, mobility, and development in *Xenopus*, we identified an existing drug, SNC80, that rapidly and reversibly slows biochemical and metabolic activities while preserving cell and tissue viability. Although SNC80 was developed as a delta opioid receptor activator, we discovered that its ability to slow metabolism is independent of its opioid modulating activity as a novel SNC80 analog (WB3) with almost 1,000 times less delta opioid receptor binding activity is equally active. Metabolic suppression was also achieved using SNC80 in microfluidic human organs-on-chips, as well as in explanted whole porcine hearts and limbs, demonstrating the cross-species relevance of this approach and potential clinical relevance for surgical transplantation. Pharmacological induction of physiological slowing in combination with organ perfusion transport systems may offer a new therapeutic approach for tissue and organ preservation for transplantation, trauma management, and enhancing patient survival in remote and low-resource locations.

Tissue and organ loss to trauma, disease, and physical injury account for a large proportion of human ailments and approximately $400 billion in annual medical burden.[1] The rapid and reversible slowing of metabolic and other physiological processes, here referred to as 'biostasis', can improve the survival of cells and organs for transplantation. This is currently accomplished clinically by lowering temperature and static cold storage is the standard of care for organ and tissue preservation; however, its long-term use can cause damage to the integrity of the graft.[1–3] Hypothermia also has been used to induce a state of biostasis clinically using *ex-vivo* machine perfusion technologies, for example, during cardiac transplant surgery. Combination of protective agents with perfusion and/or partial freezing approaches have extended preservation times in rat livers and whole pigs,[4,5] and neural modulation approaches

54 have been successful at demonstrating central control of body temperature and general
55 metabolic state.[6,7] However, both mechanical cooling and neural stimulation approaches are
56 challenging to implement in a trauma triage or resource-limited situations, which would be better
57 addressed by pharmaceutical interventions.

58 Several molecular strategies have been proposed to achieve metabolic suppression for
59 organ preservation, including modulating H_2S, AMPK, opioid receptors, microRNAs, HO-1, and
60 Nrf2.[8] H_2S exposure has been reported to induce a hypometabolic state (reduced metabolism
61 and body temperature) in a rodent model, although this was later found to be mediated in part
62 by a low baseline laboratory temperature.[9] The synthetic opioid peptide DADLE also can induce
63 hypometabolism and improve organ preservation via a delta opioid receptor (DOR) mechanism,
64 but with varied results.[10,11] Compounds that directly impact glycolysis and mitochondrial
65 respiration also have been considered for modulating organ metabolism, but many are acutely
66 toxic and not reversible, fail to protect tissues from ischemic injury, or lack drug-like properties.
67 Specifically, reduced functionality of the mitochondrial electron transport chain system without
68 the endogenous antioxidant and anti-inflammatory molecules released by hibernators can result
69 in the release of reactive oxygen species and cause tissue damage.[8]

70 Despite these efforts, there remains a large unmet need for improved tissue and organ
71 preservation approaches across multiple application areas. Thus, in the present study, we set
72 out to identify small molecules that could slow metabolism and mimic states normally induced
73 by hypothermia, hibernation, or torpor, which could be used for preservation of living cells,
74 tissues, and organs ex v*ivo*, and potentially *in vivo* as well. Specifically, we required this
75 biostasis approach to be rapidly inducible (< 1 hour) and safely reversible, with major tissue
76 functions returning to control levels within 24 hours.

77 Through survey of the literature, we identified drugs with unintended side effects, such
78 as lowering body temperature, which suggested they might have broad effects on metabolism.
79 Among these drugs was SNC80, a small molecule drug originally developed as a nonaddictive

80 pain reliever that acts independently of the mu-opioid pathway.[12] This drug caught our attention
81 because it has been shown to induce hypothermia and protect against the effects of spinal cord
82 ischemia in rodents.[12,13] To explore whether SNC80 had potential to broadly slow tissue
83 metabolism and physiology, we administered the drug to *Xenopus laevis* embryos and tadpoles,
84 which we and others have previously shown to be useful models for drug screening due to their
85 small size, extrauterine development, and skin permeability to small molecules.[14–17] The
86 Xenopus tadpoles were dosed at higher levels than dictated by SNC80's defined IC50 value,
87 with the goal of exploring the effects of SNC80 outside its known pain relief properties and
88 accentuating the drug's "off-target" effects, including hypometabolism.

89 **Demonstration of physiological slowing in *Xenopus***

90 We first assessed SNC80's impacts on mobility, metabolism, and heart activity in
91 *Xenopus*. Behavioral assessment in mobile tadpoles showed that 100 μM SNC80 slows
92 movement relative to vehicle-treated counterparts, reducing activity by approximately 50%
93 within 1 hour, which is rapidly reversible when the drug is removed (**Figure 1a**). SNC80 also
94 suppressed the rate of oxygen consumption to one-third of baseline within 3 hours of treatment
95 (**Figure 1b**) and had extreme suppressive, but fully reversible, effects on heart rate after only 1
96 hour of exposure (**Figure 1c**)**.** Oxygen consumption was reduced in immobile *Xenopus* embryos
97 treated with SNC80 as well (**Figure S1a**), suggesting that its metabolism-suppressing effects
98 are independent of the slowed movement observed in mobile tadpoles.

99 Using *in situ* Matrix-Assisted-Laser Desorption/Ionization-Time of Flight Mass
100 Spectrometry Imaging (MALDI-ToF MSI), we assessed and visualized the biodistribution of
101 SNC80 in the *Xenopus* tadpole. SNC80 was detected within 1 hour of treatment and it appeared
102 in a punctate distribution in the gastrointestinal (GI) tract, gill region and skeletal muscle
103 (**Figures 2a,b**), suggesting full-body delivery of the drug. Past lipidomic studies of hibernating
104 mammals demonstrated the importance of lipid molecules for thermal adaptation during
105 hibernation with significant alterations of lipidomic profiles being observed in liver, plasma, brain,

106 skeletal muscle and cardiac muscle during torpor as compared to the animal's active state.[18,19]
107 Similarly, MALDI-ToF MSI analysis revealed significantly higher levels of acylcarnitine and
108 cholesterol ester in SNC80-treated groups in both skeletal muscle and brain (**Figure 2c**).
109 Increased levels of long chain acylcarnitine associated with enhanced mitochondrial fatty acid
110 oxidation are observed during fasting as well as in hibernating brown bears,[20,21] and cholesterol
111 ester levels increase in hibernating ground squirrels.[22] While the increased acylcarnitine and
112 cholesterol ester levels in brain suggest a shift towards beta oxidation of fatty acids, they also
113 have been implicated in other pathways including antioxidant activity and neurotransmission.[23,24]
114 Having confirmed that SNC80 induces slowing of multiple physiological parameters in
115 the whole *Xenopus* organism, we then set out to explore the molecular basis for these effects.
116 As SNC80 is a known DOR agonist,[12,13] we next evaluated whether its effects could be
117 mediated by delta opioids. However, when we tested the DOR antagonist, naltrindole (NTI), at
118 double the concentration (200 μM), it did not block the hypometabolic effects of SNC80 (**Figure**
119 **2d**), suggesting that SNC80 modulates metabolism independent of DOR activation.

120 **Attenuating the delta opioid activity of SNC80**

121 To further test if the physiological slowing effects of SNC80 are independent of DOR
122 activation, we used a medicinal chemistry approach to explore whether we could separate its
123 metabolism slowing and DOR activities. Toward this end, we designed molecular entities void of
124 the distal basic nitrogen (N-ally group within SNC80), which we hypothesized was a critical DOR
125 pharmacophore. This effort led to the development of a novel morpholino compound, WB3
126 (**Figure 3a** & **Supplemental Synthesis Description**), which was synthesized and subsequently
127 tested for DOR binding activity using a radioligand binding assay and non-linear fitting for
128 specific binding to calculate the Hill Slope and IC50 value. A specific binding curve could not be
129 fit for SNC80 due to its high affinity and therefore its IC50 is <4.6 nM, whereas WB3 exhibited
130 an IC50 of 3,470 nM (**Figure 3b**), suggesting almost 1,000 times less DOR binding activity for
131 WB3 compared to SNC80. Subsequently, we screened WB3 in the *Xenopus* swimming and

132 heart rate assays and found that the analog retains physiological slowing properties *in vivo*
133 despite lacking delta opioid activity (**Figure 3c,d**). In fact, we observed more potent and rapid
134 effects on swimming with exposure to WB3 compared to SNC80, suggesting that the non-opioid
135 properties of SNC80 may be primarily responsible for its observed physiological effects.

136 **Enhanced preservation of whole pig hearts and limbs perfused *ex vivo***

137 Based on these intriguing findings with human Organ Chips and *Xenopus* tadpoles, we
138 set out to explore the potential clinical value of SNC80. Cardiac transplant is the gold standard
139 for treating end-stage heart failure; however, it is hindered by donor shortage, limited cardiac
140 graft preservation time, and lack of optimal organ preservation conditions. Currently, hearts are
141 allocated to patients located within 4 hours of organ removal from the donor. Thus, to explore
142 the potential utility of biostasis induction to lengthen the time between organ donation and
143 recipient surgery through pharmacological induction of a hypometabolic state, we perfused
144 surgically explanted whole porcine hearts with SNC80 using a portable, oxygenated perfusion
145 preservation device (VP.S ENCORE®) at subnormothermic temperatures (20-23°C). Prior work
146 has demonstrated that the VP.S ENCORE® enhances cardiac viability over standard of care-
147 static cold storage and hearts perfused in this device for 4 hours demonstrate similar cardiac
148 function to a healthy heart in both preclinical animal models and human deceased donor
149 hearts.[25,26]

150 We investigated the application of a biostasis inducer for preservation of the heart during
151 6 hours of perfusion in the VP.S ENCORE® device. Importantly, with SNC80 treatment, we
152 observed a rapid decline in the heart's oxygen consumption to < 50% of that observed in hearts
153 exposed to the vehicle control, which was sustained over the 6-hour preservation period (**Figure**
154 **4a**). After preservation, hearts were removed from the VP.S ENCORE® and placed in a
155 Langendorff system for reperfusion and evaluation of oxygen consumption and cardiac
156 contractility. This system assesses the left ventricular dP/dT without preload and afterload,
157 thereby allowing the evaluation of the intrinsic contractility of the left ventricle. After 30 minutes

158 of reperfusion and before defibrillation, SNC80-treated hearts had a lower oxygen consumption
159 level than vehicle treated hearts (2.39 ± 1.23 versus 4.28 ± 2.48 ml/min/100g, respectively, at
160 the 30-minute timepoint) (**Figure 4b)** that recovered to normal levels after defibrillation and with
161 increases in temperature (2.49 ± 0.53 and 2.35 ± 0.31 ml/min/100g, respectively, at 60 minutes
162 post-defibrillation) (**Figure 4c**). No evidence of substantial change in left ventricle (LV)
163 contractility or relaxation were detected in SNC80-exposed hearts, either before or after they
164 were defibrillated and exposed to epinephrine (**Figure 4d**).

165 Gene expression analysis of heart biopsy samples showed significant reduction of
166 markers of inflammation (IL-6, IL-8, TNFα), hypoxia (Hif1α), and cell death (TP53, BCL2) in
167 SNC80-treated hearts when compared to vehicle control hearts (**Figure 4e**), and no changes in
168 the mitochondrial ATP synthase marker, ATP5MC3, were observed. Histopathological
169 evaluation showed retention of normal muscle morphology (**Figure 4f**) without signs of tissue
170 edema immediately after perfusion in the VP.S ENCORE®. In some hearts treated with SNC80
171 greater waviness of muscle fibers was observed, possibly indicating a state of muscle
172 contraction.

173 Electrocardiogram (ECG) data revealed that both vehicle and SNC80-treated hearts
174 exhibited irregular beating after perfusion and prior to defibrillation. After defibrillation with
175 epinephrine, the P and QRS waveforms were visible in ECGs from 3 of 4 SNC80-treated hearts
176 (**Table S1**), suggesting that those hearts regain atrial and ventricular polarization. The pulse
177 rates of SNC80-treated hearts were at or near normal range for porcine hearts (70-120
178 beats/min) after defibrillation. Vehicle-treated hearts exhibited tachycardia following
179 defibrillation, with all exhibiting pulse rates above the normal range for porcine hearts.

180 We also tested organ preservation in porcine limbs, where prolonged ischemia after
181 amputation rapidly decreases the viability of skeletal muscle. Current preservation methods limit
182 the success of limb reimplantation due to complications from rhabdomyolysis, necrosis, and
183 reperfusion injury.[27] Again, we found that the relative metabolic rate measured during 3 hours of

184 SNC80 exposure was significantly lower compared to vehicle-treated limbs (**Figure S2a**).
185 Histopathological evaluation also showed retention of normal muscle morphology with no
186 apparent changes in muscle bundle area (**Figure S2b**) or glycogen content (**Figure S2c**)
187 suggesting that the tissue's potential for ATP synthesis was not compromised after SNC80
188 administration, although an increase in intercellular spacing was observed (**Figure S2d**). We did
189 not observe full recovery of O_2 uptake at the 3-hour time point analyzed in this study (**Figure**
190 **S2c**); however, the porcine limb contains a large amount of fat tissue that may be acting as a
191 depot for the highly lipophilic SNC80, thereby leading to extended stasis under these conditions.

192 **Elucidating potential SNC80 targets and pathways**

193 To gain insight into the molecular basis of SNC80's hypometabolic and other
194 physiological effects, we used thermal proteome profiling (TPP) to assess drug-protein binding
195 and thereby identify previously unknown molecular targets of SNC80 that might be critical for its
196 metabolism slowing activity. TPP of SNC80-treated *Xenopus* tissues revealed 19 direct and
197 indirect binding targets (**Table 1**), including proteins involved in transmembrane transport,
198 mitochondrion activity, and metabolic processes. Two potentially interesting binding targets of
199 SNC80 are the excitatory amino acid transporter 1 (EAAT1; also known as SLC1A3) and the
200 Na^+/Ca^{2+} exchanger 1 (NCX1; also known as SLC8A1), both of which have been identified in
201 cardiac tissue.[28,29] In addition to their individual functions, mitochondrial ATP production has
202 been previously reported to be stimulated through intermolecular interactions between EAATs
203 and NCXs in neurons.[30] If this complex is also present in cardiac tissue, inhibition of EAAT and
204 NCX1 could reduce cellular ATP levels,[31] and thereby play a role in slowing metabolism.
205 Specifically, the blockade of Na^+/Ca^{2+} exchange via interference with EAAT1-NCX1 interactions
206 could prevent the influx of calcium into the mitochondria that is necessary for calcium-sensitive
207 mitochondrial dehydrogenases that fuel ATP synthesis.[32] However, the mitochondrial variant of
208 NCX1 (NCLX) was not included in the *Xenopus* protein library used for TPP analysis so could
209 not be fully evaluated in this study. TPP also identified two additional SNC80-binding proteins

210 located within the mitochondrion: TOMM40 and COX6C. TOMM40 is a translocase located in
211 the outer membrane of the mitochondria that has been implicated in tissue protective effects
212 against late-onset Alzheimer disease[33] and COX6C is the terminal enzyme of the mitochondrial
213 respiratory chain, catalyzing the electron transfer from reduced cytochrome c to oxygen.
214 In addition to interaction with mitochondrial proteins, we detected binding between
215 SNC80 and enzymes involved in other metabolic processes, including alpha-L-fucosidase 2
216 (FUCA2), cysteine conjugate beta-lyase (CCBL1), retinoid isomerohydrolase (RPE65), and
217 acyl-CoA Oxidase 3 (ACOX3). SNC80 also binds to multiple membrane-spanning proteins,
218 including vacuole membrane protein 1 (VMP1) and ABCB1, an ATP-dependent translocase, in
219 addition to NCX1 and EAAT1. The drug also bound to two proteins of the immune system,
220 histocompatibility minor 13 (HM13) and pentraxin 3 (PTX3), as well as two cytoskeletal proteins,
221 calmodulin regulated spectrin associated protein family member 2 (CAMSAP2) and integrin
222 subunit alpha 7 (ITGA7). Interestingly, SNC80 also bound to four ribosomal proteins, RPL4,
223 RPL27A, RPS25, and RRP9, which are frequent targets of antibiotic and antiviral drugs.
224 Collectively, these data suggest that induction of physiological slowing by SNC80 may involve
225 simultaneous modulation of multiple pathways, with critical mechanisms involving mitochondria,
226 membrane-spanning transporters, and possibly other metabolic processes as well.

227 **Metabolic suppression in human Organ Chips**

228 To explore whether this drug also induces a state of biostasis in human cells and tissues, as
229 well as non-cardiac cells, we tested SNC80 in human organ-on-a-chip (Organ Chip) microfluidic
230 culture devices that reconstitute tissue-tissue interfaces and human organ-level physiology with
231 high fidelity in vitro.[34] The Organ Chip models reconstitute a tissue-tissue interface between
232 organ-specific epithelium and endothelium across a porous extracellular matrix-coated
233 membrane within a two-channel microfluidic device, and hence allow tissue-tissue cross talk
234 observed in vivo that is not normally present in studies with cultured cells, as previously
235 described.[35,36] In this study, we used a Gut Chip lined by Caco-2 intestinal epithelial cells

236 interfaced with HUVECs and a Liver Chip containing Huh7 liver epithelial cells interfaced with
237 LSECs, respectively. However, we modified the Organ Chip design by integrating sensors that
238 allow for live monitoring of oxygen (O_2) and transepithelial electrical resistance (TEER) (tissue
239 barrier function) (**Figure S3a**). Both Organ Chips were treated with SNC80 by flowing the drug
240 in medium for 2 days through the apical and basal channels of the chip, and then removing the
241 drug followed by 7 days of additional culture. We confirmed that the intestinal epithelial cells
242 underwent villus differentiation and accumulated mucus under these culture conditions (**Figure**
243 **S3b**), in addition to maintaining a low oxygen environment after 10-16 days of culture (**Figure**
244 **S3c**) as previously described.[35,36] The Liver Chips also produced albumin and urea at levels (5
245 and 135 µg/day/chip, respectively) (**Figure S3d,e**) that were similar to those measured in Organ
246 Chips lined by primary hepatocytes.[37,38]

247 These studies revealed that SNC80 treatment reduced the respiratory (oxygen
248 utilization) rate in the Gut Chip, resulting in an almost 6-fold increase in extracellular oxygen
249 levels after 48 hours, which then progressively returned to baseline levels during the 7-day
250 washout period (**Figure S4a**). Similar results were obtained with the more highly metabolic
251 Liver Chip with SNC80 inducing higher levels of extracellular oxygen compared to control chips
252 and this again reversed after drug washout (**Figure S4a**). Importantly, the tissues in both the
253 human Organ Chips remained healthy after 2 days treatment with SNC80 as there was no
254 significant change in barrier function (**Figures S5a,b**), cell growth (**Figure S3**), or cytotoxicity
255 (**Figures S5c,d**). Similar to the data observed in cell cultures, ATP/ADP ratio in Liver Chips was
256 significantly decreased after 24 and 48h of SNC80 treatment compared to the vehicle control
257 chips. However, ATP/ADP ratio measurements between SNC80 and vehicle control were not
258 significantly different after washout of the drug, indicating that Liver Chip tissues recover their
259 normal metabolic function up to 4 days after treatment (**Figure S4b**).

260 Collectively, these data suggest that treatment with SNC80 in these physiologically
261 relevant human cells and tissues cultured on-chip in an organ-relevant context resulted in a

262 drop in respiration, with no switch towards glycolysis or reductive carboxylation, since the levels
263 of lactate (**Figure S5e,f**) and glutamate remained unchanged in both chips (**Figure S5g,h**).
264 Thus, in this organ-like microenvironment, the tissues decrease their total ATP production in
265 presence of SNC80, which is accompanied by a global slowing of metabolism.
266

267 **Discussion**

268 Here we report the discovery that the small molecule drug, SNC80, and its analog WB3,
269 are capable of slowing of multiple physiological processes, and thereby inducing a
270 hypometabolic state without external cooling. Although there is extensive clinical experience
271 using hypothermia to cryopreserve organs during surgery (e.g., cardiac bypass) and for donor
272 transplants, comparatively little work has been done in the area of molecular induction of
273 biostasis without external cooling. We found that SNC80 reversibly suppressed metabolism
274 across multiple cell and tissue types, as well as different species and experimental models, at
275 their basal temperatures, suggesting that this approach could be appropriate for preservation of
276 a variety of cells, tissues, and organs. Critically, integrating this small molecule drug in a
277 commercial organ preservation system with whole explanted pig hearts demonstrated potential
278 for near-term translation and impact of this approach for applications relating to organ
279 preservation and surgical transplantation.

280 Initially developed as a nonaddictive pain reliever, SNC80 was previously shown to
281 induce hypothermia and protect against the effects of spinal cord ischemia in rodents,[12,13] but its
282 broad effects on metabolism were not known. In the present study, treatment with SNC80
283 slowed swimming movement and reduced oxygen consumption rates in a reversible manner in
284 *Xenopus* tadpoles, and it lowered the metabolic rate in non-mobile *Xenopus* embryos as well.
285 Importantly, SNC80 displayed similar metabolism suppressing activities that were reversible in
286 physiologically relevant human Organ Chip microfluidic devices that reconstitute organ-level
287 structures and functions in vitro. These data suggested that induction of a hypometabolic state

288 by this small molecular drug could potentially provide a new paradigm to prolong organ
289 preservation. Indeed, when we perfused explanted porcine hearts and limbs with SNC80, we
290 experimentally confirmed that this biostasis agent can slow metabolism in a whole complex
291 living organs, providing direct support for its potential integration into commercial organ
292 preservation devices that strive to extend the viability of human organs for surgical
293 transplantation.

294 SNC80 is defined as a highly selective non-peptide DOR agonist drug and other DOR
295 agonists, such as the enkephalin DADLE, have been shown to reduce metabolic demand and
296 protect against oxidative stress, thereby decreasing injury and apoptosis in perfused
297 organs.[8,10,11] Prior studies of DADLE found that the DOR pathway was required to alter
298 metabolism and provide protective effects, however, we found that SNC80 suppresses
299 metabolism via a mechanism that is independent of its DOR modulating activity. Instead, we
300 found that SNC80 interacts with multiple proteins involved in transmembrane transport,
301 mitochondrion activity, and metabolic processes. Interestingly, one of the identified targets,
302 NCX1, has been previously implicated in control of temperature compensation and autonomous
303 oscillation,[39] suggesting that it plays a key role in the regulation of biochemical reaction speed,
304 cell cycle, and other forms of biological timing, such as circadian rhythm. In addition to its
305 effects on tissues of the nervous system, multiple drugs that target Na^+/Ca^{2+} exchange by NCX,
306 such as the KBR family of drugs, were developed for the treatment of ischemia, reperfusion
307 injury, and heart arrhythmias.[40] In rats, pre-ischemic or post-ischemic treatments with KBR
308 compounds improved recovery of ventricular pump function and reduced reoxygenation-induced
309 injury as measured the reduced release of intracellular components (e.g., lactate
310 dehydrogenase).[40,41] Our results suggest that SNC80 could be acting on the NCX1
311 transmembrane protein and/or NCX1/EAAT1 pathway may result at least in part from induction
312 of a hypometabolic state.[45] Of the tissues impacted by SNC80, the observed effects were most
313 profound on *Xenopus* tadpole heart function and porcine hearts. SNC80 and other opioids have

314 been shown to decrease cardiac inotropy and contractility,[42,43] and prior work has demonstrated
315 that decreases in cardiac inotropy and contractility by opioid agonists may be mediated by
316 opioid receptor-*independent* actions of these drugs.[43] Substantial slowing of heart rate by WB3,
317 which exhibits approximately 1,000 times less delta opioid activity than SNC80, further supports
318 this claim. Similar to our findings by TPP, other investigators identified *non-opioid* receptor-
319 mediated actions of these compounds on ion channel function.[43] Changes in contractility were
320 not observed immediately after perfusion with SNC80 in porcine hearts tested here, likely
321 because the SNC80 was washed out of the tissue before contractility was measured; however,
322 future work should continue to monitor these parameters, especially at later time points.
323 Although bradycardia likely contributes to the hypometabolism observed in both systems, we
324 also see reduced metabolic rates in systems lacking cardiac cells, and thus the hypometabolic
325 activity of SNC80 we observed is not completely cardiac-specific.

326 The *Xenopus* and perfused porcine heart systems may be particularly amenable to
327 extreme slowing of cardiac output because these live tissues are surrounded by well-
328 oxygenated medium during treatment, potentially avoiding tissue injury sometimes associated
329 with hypometabolic states. However, the assumption that high oxygen content in the perfusate
330 completely precludes ischemia may not be valid. Assuming adequate flushing during recovery,
331 local vasospasm or a fat micro embolism occurring during perfusion could restrict perfusion flow
332 thereby inducing a localized hypoxic state and HIF1α expression in the tissue. SNC80 may be
333 acting in a vasodilatory capacity, thereby facilitating oxygen delivery and suppressing HIF1α
334 expression. In addition, although HIF1α is primarily known for its role in response to hypoxia, it
335 has some oxygen-independent functions and can be induced by factors other than oxygen
336 levels, such as growth factors and cytokines, which can activate its transcriptional activity even
337 under normoxic conditions. In these cases, HIF1α can regulate genes involved in cell
338 proliferation, metabolism, inflammation, and other cellular processes. Therefore, observation of

339 suppressed HIF1α, as well as the reduction of multiple inflammatory and cell death markers, in
340 the treated porcine cardiac tissue suggests a protective effect of SNC80.

341 Before considering broader applications of SNC80 or any of its analogs, such as whole-
342 body infusion during trauma or infection, it will be critical to consider impacts of this drug not
343 only on the heart but other organ systems as well. In particular, our *Xenopus* data suggest that
344 there could be substantial uptake of SNC80 in the brain, thus potentially impacting tissues of the
345 central nervous system. Therefore, future work should characterize cognitive recovery in
346 organisms receiving systemic delivery of stasis inducers. In addition, whole-body infusion
347 applications may require further pharmaceutical development, including chemical modifications
348 to SNC80 and development of targeted delivery methods to ensure clinical safety.

349 In summary, our findings demonstrate that the small molecule drugs SNC80 and WB3
350 can be used as a biostasis inducer to produce a hypometabolic state, which can provide
351 potential therapeutic value for clinical applications, such as enhanced preservation of organs.
352 The use of a biostatic compound in combination with a self-contained transport system could
353 potentially increase organ viability for sustained times *ex vivo*, thus helping to advance organ
354 and tissue preservation for surgical transplantation. The ability to induce a reversable
355 hypometabolic, suspended animation-type state rapidly through injection at the point-of-care
356 also could enable new therapeutic approaches to slow the detrimental effects of trauma and
357 acute infection, thereby increasing patient survival in military settings and space exploration, as
358 well as in civilian health emergency operations. It also may be possible to use this biostasis
359 approach to slow metabolic activities in the brain in cases of stroke or traumatic brain injury,
360 indications for which current treatments are severely limited.

361 ## Methods

362 ***Xenopus* model.** *Xenopus* embryos were fertilized at Tufts University using procedures
363 reviewed and approved by the Tufts University Institutional Animal Care and Use Committee
364 regulations and transferred to the Wyss Institute. *Xenopus* embryos and tadpoles were housed
365 at 18°C with a 12/12 h light/dark cycle in 0.1X Marc's Modified Ringer's (MMR) medium. All
366 animal experiments and procedures were reviewed and approved by the Harvard Medical
367 School (HMS) Institutional Animal Care and Use Committee regulations.

368 Drugs used in the *Xenopus* studies were dissolved in DMSO to a stock concentration of
369 10 mM and diluted to their final concentrations with a 1% DMSO concentration or less. Media
370 with dosed compound were made fresh and screening was performed in tadpoles at Stages 46-
371 50. The activity of free-swimming tadpoles during and after exposure to drugs were recorded in
372 60 mm dishes using a SONY Alpha a6100 camera with 16 mm objective (Sony Corporation,
373 Tokyo, Japan) against an illuminated background. Mobility was quantified in Matlab (Mathworks,
374 Natick, MA) by mapping differences between frames to a movement index (0 – 1), with 0
375 indicating no movement and 1 indicating maximal movement. Oxygen consumption was
376 measured during *Xenopus* exposure to drugs as a proxy for whole-organism metabolism using
377 the Firesting Optical Oxygen Meter and the Pyro Oxygen Logger software (version 3.317)
378 (Pyroscience GmbH, Aachen, Germany). Oxygen consumption for *Xenopus* embryos was
379 measured using the OxoPlate (PreSens Precision Sensing GmbH, Regensburg, Germany).
380 Oxygen consumption rate for each sample was measured using a linear fit to the oxygen
381 consumption curves in Prism (GraphPad, San Diego, CA). Heart rate was measured by
382 microscopy imaging in *Xenopus* following 1, 2, 4, or 8 hours of drug exposure. Vehicle and
383 drug-treated groups were briefly incubated in 0.01% tricaine (Syndel, Ferndale, WA) to minimize
384 tadpole movement during heart imaging. Videos of heart function were acquired using a ZEISS
385 Axio Zoom.V16 microscope and ZEN BLUE Microscopy software (version 3.1) (Carl Zeiss AG,

386 Oberkochen, Germany) at a rate of 1 frame/100 ms. Heart beats were counted automatically
387 using a custom code in Python. At the completion of experiments, *Xenopus* were euthanized by
388 immersion in 0.2% tricaine for 30 minutes, followed by fixation or bleaching and disposal.
389 **MALDI-ToF.** Tadpoles were embedded in gelatin (0.11 g/mL) and stored in -80C.
390 Embedded tadpoles were sectioned into 16 um-thick slices using a Leica CM1850 (Leica
391 Microsystems, Wetzlar, Germany) onto indium tin oxide (ITO)-coated glass slides (Bruker
392 Daltonics, Billerica, MA) and immediately placed in a vacuum desiccator before matrix
393 application (N=5 tadpoles per condition; N=3 sections/slide). Experiments were duplicated to
394 confirm the reproducibility. The matrix solution was composed of 2,4 Dihydroxybenzoic acid
395 (40mg/mL) in 0.1% formic acid, methanol/water (1:1 v/v) and was made fresh for each
396 application. The HTX-sprayer nebulizer (HTX Technologies, Carrboro, NC, USA) was used to
397 apply the matrix at 80°C at 24 passes over the sample, at a flow rate of 50μL/min, 10 psi
398 pressure and a track speed at 1,250 mm/min. Before imaging, SNC80 spotting with matrix and
399 *Xenopus* lysate was performed to determine the optimal matrix for the best S/N ratio and the
400 least ion suppression from *Xenopus* tissue and to identify which adducts were detectable for
401 each compound for imaging. *In situ* MALDI-ToF imaging was acquired using the rapifleX (Bruker
402 Daltonics, Billerica, MA), in positive ion mode at 1000 Hz in the mass range of 300-990 m/z. The
403 laser raster step spacing was set to 45 μm step size at 500 shots per pixel. External calibration
404 was performed using a red phosphorus slurry drop casted on a region of the ITO slide without
405 tissue. Preliminary processing of the data was performed using FlexAnalysis (Bruker Daltonics,
406 Billerica, MA). Images were normalized by the total ion count and baseline-corrected using Top
407 Hat algorithm with a _baseline width. After MALDI-ToF MSI acquisition, ITO slides were then
408 stained for H&E and imaged using the Cytation 5 (Agilent, Santa Clara, CA) and Epsilon
409 scanner at 3000 dpi to select regions of interest using the open-source program, Qupath.[44]
410 Mass selection windows and signal intensity analysis was conducted with SCiLS Lab (Bruker
411 Daltonics, Billerica, MA), where ions of interest, including SNC80, acylcarnitine and cholesterol

412 ester C18, were chosen with a width of ±0.25 Da. Reference peaks of target analytes were
413 based on previous MALDI-ToF work in Xenopus tissues from previous findings,[45] and during
414 spotting of target analytes with MALDI-ToF MS/MS. The mean signal intensity of the defined
415 regions of interest were obtained with each ion of interest.

416 **Radioligand binding assay.** To assess binding of WB3 to the delta opioid receptor, we
417 tested WB3 and SNC80 at 8-concentrations with 3-fold serial dilutions starting at 10 μM
418 (Reaction Biology, Malvern, PA). Binding of the tracer [3H]-DADLE (10 nM) was assessed in the
419 presence of each concentration of WB3 and SNC80 and the [3]-DADLE signal was fit to a dose-
420 response curve to quantify the Hill Slope and IC50 values.

421 **Thermal proteome profiling.** To identify drug-bound targets based on altered thermal
422 stability, *Xenopus* tadpoles were treated with either SNC80 or vehicle for 2 hours. *Xenopus*
423 were euthanized in 20X tricaine and then transferred back to their respective drug solutions to
424 ensure drug effect is not lost during heat treatment. *Xenopus* samples were incubated at 9
425 temperature points (30C, 35C, 40C, 44C, 48C, 52C, 56C, 60C, 65C) using a PCR machine (3
426 minutes heat time per condition, 3 tadpoles per condition) for both drug treated and vehicle
427 treated groups. After transfer to room temperature, liquid was aspirated from samples and
428 samples were snap frozen in liquid nitrogen. Samples were lysed in 100 μl of PBS + 0.4 % NP-
429 40 with 4 cycles of freeze/thaw. 11μl of each of the 9 temperatures were pooled in one tube and
430 samples were centrifuged at 13,000 RPM for 75 minutes, at 4C. Proteins were reduced and
431 alkylated with 10 mM DTT and 15 mM IAA for 15 minutes at 65C and 30 minutes at room
432 temperature, respectively. Proteins were then precipitated with 8 volumes of ice-cold acetone
433 and 1 volume of ice-cold methanol overnight. Digestion was carried for 4 hours in 50 mM Tris ph
434 8 + 0.75 mM Urea + 1μg trypsin/LysC at 37 Celcius with agitation. Another 1 μg of trypsin/LysC
435 was added and digestion was continued overnight. Peptides were purified by reversed phase
436 SPE and analyzed by LC-MS/MS (PhenoSwitch Bioscience, Sherbrooke, QC, Canada). LC-
437 MS/MS acquisition was performed with a ABSciex TripleTOF 6600 (ABSciex, Foster City, CA,

438 USA) equipped with an electrospray interface with a 25 µm iD capillary and coupled to an
439 Eksigent µUHPLC (Eksigent, Redwood City, CA, USA). Analyst TF 1.8 software was used to
440 control the instrument and for data processing and acquisition. Samples were acquired twice in
441 SWATH acquisition mode using gas phase fractionation. The source voltage was set to 5.5 kV
442 and maintained at 325C, curtain gas was set at 45 psi, gas one at 25 psi and gas two at 25 psi.
443 Separation was performed on a reversed phase Kinetex XB column 0.3 µm i.d., 2.6 µm
444 particles, 150mm long (Phenomenex) which was maintained at 60C. Samples were injected by
445 loop overfilling into a 5µL loop. For the 60 minutes LC gradient, the mobile phase consisted of
446 the following solvent A (0.2% v/v formic acid and 3% DMSO v/v in water) and solvent B (0.2%
447 v/v formic acid and 3% DMSO in EtOH) at a flow rate of 3 µL/min. GPF files for both acquisitions
448 were analyzed on a previously generated 3D ion library. Each GPF file was analyzed using 10
449 peptides per protein, 4 MS/MS transition per peptide, 12.5-minute RT window and 25 ppm XIC
450 width in Peakview (Sciex). The reported quantification for a protein is the sum of all the correctly
451 integrated peptides (FDR<0.05) in both GPF files.

452 **Human Cell Cultures:** Caco2 intestinal epithelial cells were grown in high glucose
453 (4.5g/L) DMEM (Gibco), 10% FBS (Gibco) and 1% penicillin/ streptomycin (Gibco) and
454 subcultured every 2-3 days at 1:6 ratio. For all experiments, cells were used between passage
455 59 and 64. HUVE cells were maintained in EBM-2 (Lonza) media with EGM-2 BulletKit (Lonza),
456 2% FBS and 1% penicillin/streptomycin (Gibco) and subcultured every 2-3 days at 1:6 ratio. For
457 all experiments, cells were used between passage 3 and 7. HuH-7 liver epithelial cells were
458 maintained in DMEM with 4.5g/L glucose (HyClone), 10% FBS and 1% penicillin/ streptomycin
459 (Gibco). We also obtained wild-type Huh7 transduced with lentivirus particle pLV[Exp]-Puro-
460 CMV>{Perceval(ns)}:T2A:mCherry/3xNLS (Vector Builder) that were used for live imaging of
461 changes in ATP/ADP ratio within these cells, which directly correlates to cellular metabolic
462 activity.[46] LSEC cells were maintained in EBM-2 (Lonza) media with EGM-2 BulletKit (Lonza),
463 2% FBS and 1% penicillin/streptomycin (Gibco).

464 **Metabolic assays**: Effluents were collected at different timepoints (baseline, 24h, 48h
465 and 1-3 days recovery after washout) throughout the exposure to SNC80 or 1:1000 DMSO
466 vehicle. After treatment, the effluent was collected and analyzed for lactate and glutamate
467 production using the Lactate-Glo™ (Promega, #J5021) and Glutamate-Glo™ (Promega,
468 #J7021) assay kits respectively as per manufacturer protocols.

469 **Cytotoxicity assay**: Cytotoxicity measurements on the Organ Chip effluents were
470 performed using the LDH-Glo™ (Promega, #J2380) as per manufacturer protocols.

471 **ATP/ADP ratio measurements**: Huh7 cells were transfected with a reporter that
472 enables direct measurements of cellular ATP:ADP ratio. The basal excitation spectrum of the
473 reporter protein was similar to that of YFP (peak around 490 nm) but it had an additional peak at
474 CFP wavelength (405 nm). As ATP levels decreased, more ADP can bind to the site,
475 decreasing the YFP/CFP ratio value. BioTek Cytation 5 Cell Imager (Agilent) was used to take
476 RFP, YFP and CFP images of each well every 20min for 180 minutes upon exposure to 100uM
477 SNC80 or 1:100 DMSO vehicle. Post processing of the images was performed using the open
478 source CellProfiler program.[47] We implemented the following pipeline to obtain quantitative
479 ATP/ADP ratio values: (1) Identify nuclei with RFP marker, (2) Define a cell as 4pixels around
480 the edge of the nuclei, (3) Measure cells YFP and CFP intensity and YFP/CFP ratio, (4) Count
481 cells per Image, (5) Track cells YFP and CFP intensity over the time course (0-3h with 20min
482 intervals), (6) Measure YFP/CFP ratio average **over all cells** per image and normalize to cell
483 count (7).

484 For the qualitative images, raw images were processed with ImageJ by using the image
485 calculator to divide yfp/cfp intensity of respective images. “Rainbow RGB” lookup table was
486 used to show the intensity changes. Tones towards the red show more intensity, higher
487 ATP/ADP ratio and higher metabolism.

488 **Organ Chips with Integrated Sensors:** To allow for live oxygen and
489 transepithelial\endothelial resistance (TEER) monitoring, we used our in-house developed and

490 fabricated microfluidic chips with integrated TEER and oxygen sensors. To mimic the in vivo-like
491 cell-cell interface on the models, a dual-channel PDMS microfluidic chip was used where the
492 apical channel is separated from the basal channel with a porous PDMS membrane. A pair of
493 TEER sensing electrodes where integrated on the apical side of the top channel and the basal
494 side of the bottom channel to measure the electrical resistance across the epithelium-
495 endothelium tissue interface. The O_2 sensing nanoparticles (OXNANO, PyroScience) were
496 integrated at four different locations in the chip: two in the apical channel and two in similar
497 locations in the bottom channel. This is to allow a fair representation of the whole chip oxygen
498 tension levels.

499 After fabrication, the chips were sterilized by plasma treatment and desiccated for 30
500 minutes. The polymeric surfaces of the membrane were then chemically functionalized using
501 ER1/ER2 buffers following Emulate^{TM} Inc. protocol and coated with extracellular matrix (ECM)
502 for 1.5-2 hours at 37°C. Gut Chip apical and basal channels were coated with 30 µg/ml
503 Collagen I (Advanced BioMatrix, Cat. no. 5005) and 100 µg/ml Matrigel (BD Biosciences) in cold
504 PBS. Liver Chip apical channel was coated with 30 µg/mL fibronectin (Corning, Cat. no.
505 356008) and 400 µg/mL Collagen I (Advanced BioMatrix, Cat. no. 5005) in cold DPBS, while the
506 basal channel was coated with 100 µg/mL Matrigel (BD Biosciences) and 200 µg/mL type I
507 collagen in cold DPBS. To create Gut Chip, HUVECs (6-8x10^6 cells/ml (P5)) were first seeded
508 on the bottom side of the permeable membrane in the basal channel and incubated for 2-3
509 hours at 37°C before seeding the Caco-2 cells (2-3x10^6 cells/ml (P78)) on the membrane in the
510 apical channel. Liver Chip was similarly created by seeding the LSEC (4-5x10^6 cells/ml (P3-8))
511 the first in the basal channel followed by seeding he Huh7 hepatocytes (2.5-3.5x10^6 cells/ml
512 (P5-15)) on the membrane in the apical channel The chips were then cultured under
513 continuous flow using the commercial culture module instrument (ZOË™ Culture Module,
514 Emulate Inc.,USA). The Gut Chips were maintained under continuous flow of 30µl/hr in the
515 apical and basal channels for 10 days before changing their respective media to differentiation-

516 promoting media (5% FBS in DMED apically and 0.5% FBS endothelial medium basally) for the
517 rest of the culture time. The Liver Chips were also maintained under continuous flow of growth
518 media at 30µl/hr in the apical and basal channels for 5-6 days before reducing the FBS content
519 to 5% in Huh7 media and 0.5% in LSEC media for inducing tissue differentiation.

520 **Human Organ Chip studies:** SNC80 was tested on the Gut Chip at day 16 of culture,
521 when the epithelium showed characteristics of matured, functional tissue and the Liver Chip was
522 tested after 7-10 days of culture. SNC80 [100µM] in the culture media was perfused through the
523 apical and basal channels of the chips at 30µl/hr, while the control chips were perfused with the
524 same culture media containing the compound's vehicle [0.5% DMSO] using the same flow
525 condition. The chips were treated with SNC80 for 48 hours before the drug was removed from
526 the media and the culture was continued for another 4 days. Both Liver and Gut Chips were
527 monitored at d-1, 0h, 3h, 24, 48h timepoints as well as day 1 and 3 after the drug washout for
528 oxygen consumption, TEER measurements, and effluent analysis. Fluorescence microscopy
529 was continuously performed from 0h throughout the treatment period and up to 3 days of
530 recovery. CellProfiler program was used to analyze ATP/ADP ratio as described above.

531 **Oxygen and TEER measurements on-chip:** Oxygen tension level measurements was
532 performed on-chip during the culture using FireSting®-O2 Optical Oxygen and Temperature
533 Meter (FSO2-C4, Pyroscience sensor technology, Germany) connected to Pryo Oxygen Logger
534 (V3.317©, Germany). TEER measurements were performed on-chip using our in-house
535 developed multiplexed TEER Tray and remotely measured from outside the incubator. A four-
536 point impedance measurement was taken on-chip periodically every 24 hours during the SNC80
537 treatment and recovery using the IviumSoft application (V4.97, Informer Technologies, Inc.). To
538 obtain the TEER of only the epithelial-endothelial tissue interface, the measured impedance at
539 100Hz was subtracted from the impedance at 100kHz and reported as the tissue impedance(Ω)
540 throughout the culture and in response to different stimuli as we reported previously.[48]

541 **DNA damage and proliferation assays**: The Click-IT™ EdU cell proliferation kit
542 (Thermofisher, #C10337) was used to assess cell proliferation in the formaldehyde-fixed chips
543 and DNA damage was assessed by staining anti-H2AX antibody (Novus Bio NB100-2280).
544 **Urea Assay**: Urea nitrogen was measured using a colorimetric assay (urea nitrogen
545 test, Stanbio Laboratory), whereby undiluted liver chip effluents were added to a 96 well plate
546 and mixed with the kit's working reagents as per manufacturer protocol.
547 **Albumin Assay**: Liver albumin production was measured using an enzyme-linked
548 immunosorbent assay (Bethyl Laboratories). Liver Chip effluents were diluted 1:100 in buffer
549 before being plated in the kit's 96 well plate, aside from standard wells with dilution series of
550 known albumin concentration solution. We followed manufacturer protocol to perform the
551 sandwich ELISA assay and measure absorbance at 450nm.
552 **Porcine heart ex vivo perfusion studies:** After induction of anesthesia and preparation
553 for clean, non-survival surgery, a median sternotomy was performed followed by longitudinal
554 incision in the pericardium to expose the heart and the great vessels. Following blunt dissection
555 and exposure of the vena cava, aorta and the brachycephalic artery, the superior vena cava,
556 and azygos vein was ligated and divided. The brachycephalic artery was catheterized for
557 infusion of cardioplegia solution. The inferior vena cava was clamped and divided proximal to
558 the clamp. Two or three pulmonary arteries were incised for decompression of the left side of
559 the heart. The aorta was immediately clamped and 10-15 ml/kg of body weight of cold (2-4°C)
560 cardioplegia solution (del Nido without lidocaine, 3 L) was infused at a pressure of 70-80mmHg
561 to stop the heart. Cold 4°C saline and ice were poured over the heart and the accumulated
562 fluids from the thoracic cavity were removed by suction. Following cessation of myocardial
563 function, the heart was removed from the chest by further dissection and division of the
564 pulmonary vessels and aorta distal to the clamp. The heart was cooled in a surgical bowl with
565 cold saline for inspection and preparation for perfusion. All procedures were conducted under

566 the UT Health San Antonio approved Institutional Animal Care and Use Committee (IACUC)
567 protocol 20210080AR.

568 After the heart was removed and placed in a surgical bowl, the aorta and the coronary
569 sinus were cannulated using sterile zip ties. The heart was placed into the VP.S ENCORE®
570 perfusion device filled with 3 L of Krebs-Henseleit buffer supplemented with 20PEG and
571 hemoglobin-based oxygen carrier (HBOC; Hemoglobin Oxygen Therapeutics, LLC, Souderton,
572 PA). The heart was perfused with a pressure of approximately <20 mmHg resulting in a
573 coronary perfusate flow of 50-100 mL/min at a 20-23°C temperature. Hearts were immediately
574 treated with 3 mL of 3% lactic acid containing 135 mg of SNC80 (100 μM final concentration),
575 administered through the arterial line followed by the 3 mL of Krebs-Henseleit flush. Post drug
576 administration, the heart continued to be perfused for additional 6 hours.

577 Two oxygen probes (Pyro FireSting™) collected oxygen partial pressure (mmHg) data of
578 the solution before entering the coronary arteries (arterial) and after exiting the cannulated
579 pulmonary artery (venous), whereas flow was measured using the Sensirion flow meter. Oxygen
580 consumption was captured using the following formula, (([O_2]a- [O_2]v)/100 * Q)/heart weight) *
581 100. [O_2]a and [O_2]v are defined as oxygen content of arterial and venous perfusate
582 respectively. [O_2] was calculated as (1.34 * Hb* SO_2) + (K * pO_2); where 1.34 is mL O_2 / Hb
583 (g), Hb is the concentration of hemoglobin measured in g/dL, SO_2 is the oxygen saturation ratio
584 calculated using the equation developed by Severinghaus,[49] K is the oxygen solubility
585 coefficient adjusted for the perfusate temperature at every data point, pO_2 is the partial pressure
586 of oxygen in mmHg for the perfusate sample, and Q is coronary flow in mL/min.

587 After preservation, hearts were placed on a Langendorff system with a perfusate mixture
588 of 1:1 porcine blood and Krebs-Henseleit buffer. Myocardial oxygen consumption
589 (MVO_2 mLO_2 /min / 100g) was calculated during an initial 30 min of rewarming stage (before
590 defibrillation) and after defibrillation using two oxygen probes (Pyro FireSting™, placed in

591 arterial and venous effluent). Oxygen consumption was [53]calculated using the same approach
592 described for the VP.S ENCORE® perfusion stage. The left ventricular function was expressed
593 as dP/dT (mmHg/sec) measured by placing a pressure catheter (Millar, 5F) in the left ventricle.
594 Data was analyzed using PowerLab (LabChart 8.1.16) blood pressure analyzer. Data was
595 selected from the left ventricular pressure waveform as the average of 30 beats after
596 stabilization (approx. 30 minutes after defibrillation). Contractility after ionotropic support was
597 measured less than 5 minutes after administration of epinephrine (0.5mg injected arterial). End
598 diastolic pressure of the left ventricle was maintained 5.14 +/- 1.89 mmHg through administering
599 perfusate directly into the left ventricle through the pulmonary veins and venting to
600 atmosphere.

601 ECG data were obtained through the placement of leads on the apex (positive), right
602 atrial appendage (negative), and aortic root (ground). Data was collected through the PowerLab
603 system and 30-second time intervals were selected for all groups before the flush, before
604 defibrillation, at native contraction, and after epinephrine drug administration. The ECG
605 amplitude (mV) was analyzed using LabChart Pro (v8.1.19) peak analysis detection at
606 approximate time points 10min (before flush) and 30min (before defibrillation) to detect the
607 average amplitude of electrical activity without full contraction. LabChart Pro (v8.1.19) ECG
608 Analysis detection was used at time points 35min (Epinephrine) and 60min (Native) to detect
609 the average amplitude of the QRS complex with contraction. The native QRS Interval (s) and ST
610 Height (mV) was averaged over a 30-second time interval using LabChart Pro (v8.1.19) ECG
611 Analysis.

612 Total RNA from cardiac tissue biopsies (2.5 mm) were extracted following the RNeasy
613 Mini kit (Qiagen) according to the manufacturer's instructions. The concentration of total RNA
614 was evaluated and measured at 260/280nm by spectrophotometer (NanoVue Plus, GE
615 Healthcare). Synthesis of cDNA was performed from 0.5 µg of total RNA, which was reverse
616 transcribed using (iScript cDNA Synthesis Kit, Bio-Rad) according to the manufacturer's

617 instructions. Gene-specific pre-designed oligonucleotide primers were purchase from Sigma.
618 qRT-PCR was done using SsoAdvanced Universal SYBR Green Supermix and SFX96 Touch
619 real time PCR detection system (Bio-Rad, T100 Thermal Cycler). The cycling parameters were
620 as follows: initial denaturation 95°C, 2 min; denaturation 95°C, 5 s; annealing/extension 60°C,
621 30 s; number of cycles 40; melt curve 65°-95°C (0.5°C increments). The comparative CT (2-
622 ΔΔCT) method was used for all quantification. Values were normalized to the Gapdh
623 housekeeping gene.

624 **Porcine limb ex vivo perfusion studies:** Hindlimbs (N=8) were procured via protocol
625 tissue sharing at the Joint Base San Antonio Clinical Investigation and Research Support
626 (CIRS) building, following IV Pentobarbital euthanasia, 100 mg/kg from a host protocol. Host
627 protocol animals were treated with the same surgical manipulations and no chemicals or drugs
628 were introduced experimentally prior to euthanasia. Following euthanasia, a curvilinear incision
629 was made around the hindlimb circumferentially. Subsequently, the neurovascular pedicle in the
630 medial hindlimb was identified and carefully dissected out to preserve the vascular bundle. The
631 pedicle was then divided at the origin of the artery and vein to preserve maximal length of the
632 vessels. Hindlimb bone was separated using a Gigli Saw. Hindlimbs were cannulated through
633 the femoral artery and underwent immediate arterial flush with up to 200-400 mL heparinized-
634 saline solution (10,000 units of heparin per 1L of saline), until venous outflow was clear.
635 Additionally, the femoral vein was cannulated for measurement and collection of venous outflow
636 samples.

637 Limbs were divided into two groups, control (N=3) and experimental SNC80 (N=5). All
638 hindlimbs were connected to the ENCORE® head for perfusion via the cannulated femoral
639 artery. The femoral vein was cannulated for obtaining venous samples. Hindlimbs were
640 perfused with oxygenated Krebs-Henseleit (KH) at ambient temperature. Arterial and venous
641 pO2 were assessed hourly using a commercial blood gas analyzer (ALB1000 by Radiometer,
642 Brea, California USA). Oxygen consumption was calculated from A-V differences obtained from

643 arterial and venous blood gas readings. After 3 hours of perfusion (baseline), torpor inducing
644 compound SNC80 (44.96 µg/ml) was administered via the femoral artery to the experimental
645 group (SNC80) (N=5) and an equal volume of the sham vehicle to the control limbs (N=3)
646 followed by and additional 3 hours of perfusion (drug). The hind limbs were then removed from
647 the perfusor and flushed with fresh KH perfusate and replaced into the perfusor containing fresh
648 KH solution (flush). The perfusion then resumed for an additional 6 hours. The hindlimbs were
649 weighed pre and post perfusion. Biopsy tissue samples were taken at baseline (pre-ENCORE®),
650 and before and after the administration of the SNC80 compound for RNA-Seq analysis and
651 histological evaluation.

652 Biopsies for histopathology were obtained superficially from the rectus femoris muscle
653 bundle immediately after amputation and then 24 hours after the perfusion period. Biopsies
654 were stored in 10% formalin for 24 hours and then stored for 3 days in 70% ethanol and
655 embedded in paraffin. The samples were sectioned into 5µm slides and stained with
656 hematoxylin and eosin (H&E) to evaluate tissue morphology, intracellular distance, muscle
657 bundle area, and Periodic Acid-Schiff to evaluate glycogen content. Histological analysis was
658 performed by visualizing slides under a light microscope (AM Scope T670Q, Irvine, California)
659 and capturing images using a high-definition camera (AM Scope Model# MU2003B1, Irvine,
660 California). From each slide, 10 digital images from randomly selected fields were obtained at
661 10x magnification. The images were de-identified and evaluated for intracellular distance,
662 muscle bundle area and glycogen content by two independent reviewers using Image J
663 software (v.1.51.).

664 **Statistical analysis.** All graphing and statistical analyses were performed with Prism 9
665 (GraphPad Software Inc., La Jolla, CA, USA) with a (two-sided) significance level of 0.05.
666 Statistical tests and corrections for multiple comparisons are described in each figure panel.
667

668 **Data availability statement**

The proteomics data reported in this paper have been deposited in the Mass Spec Interactive Virtual Environment, MassIVE, (accession no. MSV000091410). All other data are available within the paper and its Supplementary Information files.

Software availability statement

A custom Python script was used to automatically count heart beat in *Xenopus* tadpoles. This code can be accessed on GitHub: https://github.com/k-shcherb/heart_seg.

Acknowledgements

The authors gratefully acknowledge funding from the Army Research Office/DARPA under Cooperative Agreement Number W911NF-19-2-0027. The views and conclusions contained in this document are those of the authors and should not be interpreted as representing the official policies, either expressed or implied, of the Army Research Office/DARPA or the U.S. Government. The U.S. Government is authorized to reproduce and distribute reprints for Government purposes notwithstanding any copyright notation herein. M.P.O. acknowledges financial support from the Margarita Salas postdoctoral grant (UNI/551/2021). We thank E. Switzer for Xenopus embryo fertilization; R. Colon, S. Sundar, and E. Lederer for Xenopus embryo husbandry and transport organization; members of the Levin Lab, Tufts University for useful discussions; and R. Gould for help with database extraction. Image analysis workflows were created in consultation with D. Stirling and B. Cimini of the Broad Institute Imaging Platform.

Author Contributions

R.N., M.Su., and D.E.I. conceived of and directed the work. M.M.S., H.F., E.G., A.K., S.K., M.P.O., K.She., and T.L. performed *Xenopus* studies with guidance from R.N. and M.Lev. R.M. developed and maintained engineered components for *Xenopus* assays. H.F., M.M.S., A.K.,

M.P.O., and T.T. analyzed *Xenopus* data. T.L. and M.Lew. performed MALDI-TOF experiments and analyzed the data. B.C., K.P., and Z.I. performed in vitro and Organ Chip studies and analyzed data with guidance from A.M.S. S.M. and K.Shc. designed, assembled, and maintained custom microscopy equipment for Organ Chip imaging. K.Shc. analyzed imaging data from tadpole and in vitro experiments. S.L. oversaw compound management and material transfers. J.M. designed novel chemical entities. Porcine heart experiments were conceived and directed by R.V. and L.B and experiments were designed and interpreted by R.V., L.B., and K.A. Porcine heart data analysis was performed by R.V., L.B., K.A, E.C., R.L., I.C., Z.M., and D.D.C. Porcine heart data was acquired by K.A, E.C., R.L., I.C., and Z.M. Porcine limb studies were conceived and directed by R.V., L.B., E.W., and T.P. Porcine limb surgeries were performed by J.Y., O.P., and J.S. Porcine limb sampling and data analysis were performed by R.V., L.B., J.P., D.W., Z.H., C.H. and J.C.H. M.M.S., B.C., K.P., Z.I., T.L., K.A., R.N. and D.E.I. drafted the manuscript and all authors reviewed and provided critical input for the manuscript.

Competing Interests

D.E.I. is a founder, board member and Scientific Advisory Board chair of, and holds equity in, Emulate Inc. M.Le., R.N., M.M.S., E.G., T.T., and D.E.I are inventors on a relevant patent application held by Harvard University (PCT/US2021/012626). R.N., E.G., M.Le., and D.E.I. hold equity in Unravel Biosciences, Inc.; R.N. and D.E.I. are members of its board of directors; M.Le. and D.E.I. are members of its scientific advisory board; and R.N. and E.G. are current employees of the company. R.V., L.B., K.A, E.C., R.L., I.C., and Z.M are employees of Vascular Perfusion Solutions. D.E.I. is a member of its scientific advisory board. The remaining authors declare no competing interests.

References

1. Vela, R. J., Jessen, M. E. & Peltz, M. Ice, ice, maybe? Is it time to ditch the igloo cooler? Benefits of machine perfusion preservation of donor hearts. *Artificial Organs* vol. 44 220–227 Preprint at https://doi.org/10.1111/aor.13599 (2020).
2. Petrenko, A. *et al.* Organ Preservation into the 2020s: The Era of Dynamic Intervention. *Transfusion Medicine and Hemotherapy* vol. 46 151–172 Preprint at https://doi.org/10.1159/000499610 (2019).
3. Guibert, E. E. *et al.* Organ preservation: Current concepts and new strategies for the next decade. *Transfusion Medicine and Hemotherapy* vol. 38 125–142 Preprint at https://doi.org/10.1159/000327033 (2011).
4. Andrijevic, D. *et al.* Cellular recovery after prolonged warm ischaemia of the whole body. *Nature* (2022) doi:10.1038/s41586-022-05016-1.
5. Tessier, S. N. *et al.* Partial freezing of rat livers extends preservation time by 5-fold. *Nat Commun* **13**, 4008 (2022).
6. Hrvatin, S. *et al.* Neurons that regulate mouse torpor. *Nature* **583**, 115–121 (2020).
7. Takahashi, T. M. *et al.* A discrete neuronal circuit induces a hibernation-like state in rodents. *Nature* **583**, 109–114 (2020).
8. Dou, M., Lu, C. & Rao, W. Bioinspired materials and technology for advanced cryopreservation. *Trends in Biotechnology* vol. 40 93–106 Preprint at https://doi.org/10.1016/j.tibtech.2021.06.004 (2022).
9. Blackstone, E., Morrison, M. & Roth, M. B. H2S induces a suspended animation-like state in mice. *Science (1979)* **308**, 518 (2005).
10. Beal, E. W. *et al.* [D-Ala 2 , D-Leu 5] Enkephalin Improves Liver Preservation During Normothermic Ex Vivo Perfusion. *Journal of Surgical Research* **241**, 323–335 (2019).
11. Ratigan, E. D. & McKay, D. B. Exploring principles of hibernation for organ preservation. *Transplantation Reviews* vol. 30 13–19 Preprint at https://doi.org/10.1016/j.trre.2015.08.002 (2016).
12. Rawls, S. M., Hewson, J. M., Inan, S. & Cowan, A. Brain delta2 opioid receptors mediate SNC-80-evoked hypothermia in rats. *Brain Res* **1049**, 61–69 (2005).
13. Horiuchi, T. *et al.* The Effects of the δ-Opioid Agonist SNC80 on Hind-Limb Motor Function and Neuronal Injury After Spinal Cord Ischemia in Rats. *Anesth Analg* **99**, 235–240 (2004).
14. Sperry, M. M. *et al.* Enhancers of host immune tolerance to bacterial infection discovered using linked computational and experimental approaches. *Advanced Science* (2022).
15. Novak, R. *et al.* Target-agnostic discovery of Rett Syndrome therapeutics by coupling computational network analysis and CRISPR-enabled in vivo disease modeling. *bioRxiv* (2022) doi:10.1101/2022.03.20.485056.
16. Schmitt, S. M., Gull, M. & Brändli, A. W. Engineering Xenopus embryos for phenotypic drug discovery screening. *Adv Drug Deliv Rev* **69–70**, 225–246 (2014).
17. Sullivan, K. G. & Levin, M. Inverse drug screening of bioelectric signaling and neurotransmitter roles: Illustrated using a Xenopus tail regeneration assay. *Cold Spring Harb Protoc* **2018**, 154–163 (2018).
18. Giroud, S. *et al.* Lipidomics reveals seasonal shifts in a large-bodied hibernator, the brown bear. *Front Physiol* **10**, (2019).
19. Kolomiytseva, I. K. Lipids in mammalian hibernation and artificial hypobiosis. *Biochemistry (Moscow)* vol. 76 1291–1299 Preprint at https://doi.org/10.1134/S0006297911120029 (2011).
20. Soeters, M. R. *et al.* Muscle acylcarnitines during short-term fasting in lean healthy men. *Clin Sci* **116**, 585–592 (2009).

21. Welinder, K. G. *et al.* Biochemical foundations of health and energy conservation in hibernating free-ranging subadult brown bear ursus arctos. *Journal of Biological Chemistry* **291**, 22509–22523 (2016).
22. Otis, J. P., Sahoo, D., Drover, V. A., Yen, C. L. E. & Carey, H. v. Cholesterol and lipoprotein dynamics in a hibernating mammal. *PLoS One* **6**, (2011).
23. Jones, L. L., McDonald, D. A. & Borum, P. R. Acylcarnitines: Role in brain. *Progress in Lipid Research* vol. 49 61–75 Preprint at https://doi.org/10.1016/j.plipres.2009.08.004 (2010).
24. Petrov, A., Kasimov, M. & Zefirov, A. Brain Cholesterol Metabolism and Its Defects: Linkage to Neurodegenerative Diseases and Synaptic Dysfunctio. *Acta Naturae* **8**, 58–73 (2016).
25. Veraza, R. *et al.* (872) Preclinical Evaluation of the VP.S ENCORE^{TM} Cardiac Preservation Device. *The Journal of Heart and Lung Transplantation* **42**, S379 (2023).
26. Andrijauskaite, K. *et al.* (399) Novel Portable Hypothermic Perfusion Preservation Device Enhances Cardiac Output of Donated Human Hearts. *The Journal of Heart and Lung Transplantation* **42**, S188 (2023).
27. Kaltenborn, A. *et al.* Ex vivo limb perfusion for traumatic amputation in military medicine. *Mil Med Res* **7**, (2020).
28. Ralphe, J., Segar, J., Schutte, B. & Scholz, T. Localization and function of the brain excitatory amino acid transporter type 1Bin cardiac mitochondria. *J Mol Cell Cardiol* **37**, 33–41 (2004).
29. Maiolino, M. *et al.* Essential role of the Na+-Ca2+ exchanger (NCX) in glutamate-enhanced cell survival in cardiac cells exposed to hypoxia/reoxygenation. *Sci Rep* **7**, 13073 (2017).
30. Magi, S. *et al.* Glutamate-induced ATP synthesis: Relationship between plasma membrane Na+/Ca2+ exchanger and excitatory amino acid transporters in brain and heart cell models. *Mol Pharmacol* **84**, 603–614 (2013).
31. Magi, S., Piccirillo, S. & Amoroso, S. The dual face of glutamate: from a neurotoxin to a potential survival factor—metabolic implications in health and disease. *Cellular and Molecular Life Sciences* vol. 76 1473–1488 Preprint at https://doi.org/10.1007/s00018-018-3002-x (2019).
32. Magi, S., Piccirillo, S. & Amoroso, S. The dual face of glutamate: from a neurotoxin to a potential survival factor—metabolic implications in health and disease. *Cell. Mol. Life Sci.* **76**, 1473–1488 (2019).
33. Chiba-Falek, O., Gottschalk, W. K. & Lutz, M. W. *The effects of the TOMM40 poly-T alleles on Alzheimer's disease phenotypes*. (2018).
34. Ingber, D. E. Human organs-on-chips for disease modelling, drug development and personalized medicine. *Nature Reviews Genetics* vol. 23 467–491 Preprint at https://doi.org/10.1038/s41576-022-00466-9 (2022).
35. Si, L. *et al.* A human-airway-on-a-chip for the rapid identification of candidate antiviral therapeutics and prophylactics. *Nat Biomed Eng* (2021) doi:10.1038/s41551-021-00718-9.
36. Kim, H. J., Li, H., Collins, J. J. & Ingber, D. E. Contributions of microbiome and mechanical deformation to intestinal bacterial overgrowth and inflammation in a human gut-on-a-chip. *Proc Natl Acad Sci U S A* **113**, E7–E15 (2016).
37. Choi, Y. Y., Kim, J., Lee, S. H. & Kim, D. S. Lab on a chip-based hepatic sinusoidal system simulator for optimal primary hepatocyte culture. *Biomed Microdevices* **18**, (2016).
38. Ewart, L. *et al.* Qualifying a human Liver-Chip for predictive toxicology: Performance assessment and economic implications. *bioRxiv* 2021.12.14.472674 (2021) doi:10.1101/2021.12.14.472674.

39. Kon, N. *et al. Na + /Ca 2+ exchanger mediates cold Ca 2+ signaling conserved for temperature-compensated circadian rhythms*. *Sci. Adv* vol. 7 http://advances.sciencemag.org/ (2021).
40. Shah Amran, M., Homma, N. & Hashimoto, K. *Pharmacology of KB-R7943: A Na +-Ca 2+ exchange inhibitor-sion arrhythmia-KB-R7943-Na +-Ca 2+ exchange (NCX1-3)-NCX inhibitors-Ni 2+-SEA0400-SN-6*. (2003).
41. Schafer, C. *et al. Role of the reverse mode of the Na / Ca exchanger in reoxygenation-induced cardiomyocyte injury*. *Cardiovascular Research* vol. 51 www.elsevier.com/locate/cardiores (2001).
42. Headrick, J. P., See Hoe, L. E., Du Toit, E. F. & Peart, J. N. Opioid receptors and cardioprotection-'opioidergic conditioning' of the heart Correspondence LINKED ARTICLES. *Br J Pharmacol* **172**, 2026–2050 (2015).
43. Pugsley, M. K. The diverse molecular mechanisms responsible for the actions of opioids on the cardiovascular system. *Pharmacol Ther* **93**, 51–75 (2002).
44. Bankhead, P. *et al.* QuPath: Open source software for digital pathology image analysis. *Sci Rep* **7**, (2017).
45. Goto-Inoue, N., Kashiwagi, A., Kashiwagi, K. & Mori, T. Metabolomic approach for identifying and visualizing molecular tissue markers in tadpoles of Xenopus tropicalis by mass spectrometry imaging. *Biol Open* **5**, 1252–1259 (2016).
46. Berg, J., Hung, Y. P. & Yellen, G. A genetically encoded fluorescent reporter of ATP:ADP ratio. *Nat. Methods* **6**, 161–166 (2009).
47. Stirling, D. R. *et al.* CellProfiler 4: improvements in speed, utility and usability. *BMC Bioinformatics* **22**, (2021).
48. Henry, O. Y. F. *et al.* Organs-on-chips with integrated electrodes for trans-epithelial electrical resistance (TEER) measurements of human epithelial barrier function. *Lab Chip* **17**, 2264–2271 (2017).
49. Severinghaus, J. W. *Simple, accurate equations for human blood 02 dissociation computations*. (1979).

851 ## Figure Legends

852 **Figure 1. SNC80 treatment in *Xenopus* tadpoles. a.** Swimming activity of *Xenopus*
853 during 100μM SNC80 or vehicle treatment. Data represent the mean±SD of n=3 replicates, with
854 10 tadpoles per replicate. **b.** Oxygen consumption rate for *Xenopus* treated with SNC80 or
855 vehicle controls. N=5 medium only, n=7 vehicle and n=9 SNC80, with each data point
856 representing the cumulative oxygen consumption for 5 tadpoles. **c.** Heart rate in SNC80 and
857 vehicle-treated *Xenopus* (n=10 tadpoles/group). Statistical comparisons were performed using a
858 Brown-Forsythe and Welch ANOVA test with a Dunnett correction for multiple comparisons (**b**)
859 and a 2-way ANOVA (treatment x timepoint) with Tukey correction for multiple comparisons (**c**).
860 Bar plots show the mean±SD of each group.

861 **Figure 2. SNC80 uptake and activity at the delta opioid receptor. a.** Distribution of
862 SNC80 in *Xenopus* tadpoles after 1 and 2 hours of compound exposure. **b.** Uptake of SNC80 in
863 the tadpole skeletal muscle, GI tract, and gills at 1 and 2 hours of exposure. **c.** Levels of
864 acylcarnitine and cholesterol ester in the skeletal muscle and brain after 1 hour of SNC80
865 treatment. *In vivo* distributions of SNC80 and lipid levels measured from N=5 tadpoles per
866 condition; N=3 sections/slide. **d.** Oxygen consumption in *Xenopus* tadpoles treated with SNC80,
867 the delta opioid antagonist naltrindole, or a combination of SNC80 and naltrindole. N=3
868 replicates/group with each data point representing the cumulative oxygen consumption from 5
869 tadpoles. Statistical comparisons were performed using a two-way ANOVA (time x tissue
870 region) with Sidak's correction for multiple comparisons (**b**), multiple unpaired t-tests for each
871 tissue region with FDR correction (**c**), and a Welch ANOVA test with Dunnett correction for
872 multiple comparisons between vehicle and each treatment group (**d**). Bar plots show the
873 mean±SD of each group.

874 **Figure 3. Design and *in vivo* screening of novel analog WB3. a.** Molecular structures
875 for SNC80 and novel compound WB3. **b.** Percent specific binding of the delta opioid receptor

radioligand [3H]-DADLE in the presence of SNC80 and WB3. c. Swimming activity of *Xenopus* during 100μM WB3, SNC80, or vehicle treatment. Data represent the mean±SD of n=2 replicates, with 10 tadpoles per replicate. **d.** Heart rate in WB3 and vehicle-treated *Xenopus* (n=10 tadpoles/group). Statistical comparisons were performed using a two-way ANOVA (group x timepoint) with Sidak correction for multiple comparisons (**d**). Bar plots show the mean±SD of each group.

Figure 4. Preservation of porcine cardiac grafts with SNC80 over 6 hours. a. Oxygen consumption for vehicle and SNC80-treated cardiac grafts perfused in the VP.S ENCORE® device (n=3 hearts/group). **b.** Oxygen consumption during cardiac reperfusion on the Langendorff system before defibrillation (n=3 vehicle and n=3 SNC80 hearts). **c.** Oxygen consumption measured on the Langendorff system after defibrillation (n=3 vehicle and n=3 SNC80 hearts). **d.** Left ventricle (LV) contractility and relaxation before and after defibrillation and tissue exposure to epinephrine (n=3 vehicle and n=2 SNC-treated hearts). **e.** Gene expression analysis of heart biopsy samples for vehicle and SNC80-treated cardiac grafts (n=2 hearts/group; 3 technical replicates each). **f.** Light microscopic views of H&E-stained histological sections of heart biopsies (20x magnification) after 6 hours of perfusion. Statistical comparisons were performed using multiple unpaired t-tests between SNC80 and vehicle-treated cardiac grafts (**a,b,c**), two-way ANOVA with Sidak correction for multiple comparisons between SNC80 and vehicle-treated cardiac grafts (**d**), and unpaired t-tests between SNC80 and vehicle for each gene of interest (**e**). Data represent the mean±SD.

Tables

Table 1. SNC80 protein binding targets identified by thermal proteome profiling.

Supplemental Figure Legends

901 **Figure S1. Metabolic measurements in SNC80-treated *Xenopus* embryos.** Oxygen
902 consumption rate in *Xenopus* embryos treated with SNC80 (n=3-4 replicates/group). Statistical
903 comparisons were performed using a Brown-Forsythe and Welch ANOVA test with Dunnett
904 correction for multiple comparisons between untreated and each treatment group. Data
905 represent the mean±SD.

906 **Figure S2. Preservation of whole porcine limbs with SNC80. a.** The relative
907 metabolic rate at baseline is not statistically significantly different between control (n=3) and
908 SNC80 (n=5) injected limbs. Metabolic rate is reduced during the treatment and washout
909 phases for SNC80 relative to controls. **b.** Mean muscle bundle area between T0 before SNC80
910 administration and at T3 after SNC80 administration and histographs of limb biopsy (20x
911 magnification) at T0 before SNC80 administration and T3 after SNC80 administration. Muscle
912 bundle area is not affected by the administration of SNC80. **c.** Optical density between T0
913 before SNC80 administration and at T3 after SNC80 administration and histographs of limb
914 biopsy (20x magnification) at T0 before SNC80 administration and T3 after SNC80
915 administration. Optical density is not affected by the administration of SNC80. **d.** Mean
916 intracellular distance during T0 before SNC80 administration versus T3 after SNC80
917 administration and histographs of limb biopsy (10x magnification) at T0 before SNC80
918 administration and T3 after SNC80 administration. Red arrows indicate intracellular distance
919 measured. Intracellular distance increases after the administration of SNC80. Statistical
920 comparisons were performed using a mixed-effects analysis with a Sidak's test for multiple
921 comparisons (a) and Welch's t-test (b-d). Data represent the mean±SD.

922 **Figure S3. Characterization of human Gut and Liver Chips with integrated sensing**
923 **technology. a.** Illustration of the sensor-integrated OOC unit connected to reservoir pod for
924 automatic operation of fluid flow using pneumatic pressure (left). Inset shows a schematic of the
925 top and bottom views of the sensor-chip-PCB compartment showing locations of TEER

926 electrodes and O_2 sensors in the apical and basal channels. Four O_2 sensing spots were added
927 to the channels - two in the top and two in the bottom channels for across the chip
928 measurement. Electrode connectors are necessary for remote TEER sensing. **b.** Phase contrast
929 images of Caco-2 cells seeded on sensor-chip at day 1, and 10 of culture (top) and Huh7 cells
930 seeded on sensor-chip at day 1 and 10 (middle). Fluorescent images of liver chip at day 1 and
931 10 of the transduced nuclear marker (bottom) **c.** Percentage of O2 level (black) and TEER
932 impedance values (gray) on sensor Liver Chip during 10 days of culture. **d**. Average albumin
933 production of Liver Chips at day of experiment start (day 7-10 of culture). **e**. Average urea
934 production of Liver Chips at day of experiment start (day 7-10 of culture). **f.** Representative
935 immunofluorescence images of the sensor Gut Chip (left) and Liver Chip (right) epithelium
936 stained with DNA damage marker (H2AX) and nuclei (DAPI) for vehicle control and SNC80
937 treated tissues after 7 days recovery. **g.** Quantitative analysis of proliferation and DNA damage
938 stains on Gut and Liver Chips after 48h of treatment and 7-day recovery to 100μM SNC80 (2-3
939 biological replicates/group/marker). Statistical comparisons were performed using multiple
940 unpaired t-tests for each marker with FDR correction. Data represent the mean±SD.

941 **Figure S4. SNC80 treatment in human Organ Chips. a.** Monitoring changes in O_2
942 levels in human Gut (dotted lines; n=6 Chips/group) or Liver (straight lines; n=15-16
943 Chips/group) Chips throughout the treatment with 100 μM SNC80 (0-48h) and recovery (48-
944 120h) versus vehicle control Chip. **b.** Graph showing the quantitative drop in ATP/ADP ratio of
945 Liver Chip treated for 48h with 100μM SNC80 or Vehicle control as well as 2 days recovery after
946 drug washout (n=5 control and n=3 SNC80 Chips). Statistical comparisons were performed
947 using multiple unpaired t-tests for each timestamp with multiple comparison between control
948 and treated cells. Data represent the mean±SD.

949 **Figure S5. Metabolic measurements of Gut and Liver Chip systems treated with**
950 **SNC80. a.** Monitoring the percentage change in barrier function of Gut (n=6 Chips/group) or **b**.

951 Liver Chip (n=9 Chips/group) with time during treatment with 100μM SNC80 (0-48h) and
952 recovery (48-120h) versus vehicle control Chip. **c**. Cytotoxicity measured for the Gut and **d.**
953 Liver Chips during treatment and recovery. **e**. Graph depicting the amount of lactate measured
954 in effluents of Gut and **f**. Liver Chips post recovery (day 7 for Gut and day 5 for Liver) for
955 SNC80-treated (red) or vehicle control (black) Chips. **g**. Graph showing the glutamate measured
956 in effluents of Gut or **h**. Liver Chips during SNC80 (red) or vehicle (black) treatment and post
957 recovery (day 7). For each measurement, statistical comparisons were performed using multiple
958 unpaired t-tests at each timepoint and FDR correction for multiple comparisons. Data represent
959 the mean±SD.

960 **Table S1. Clinical interpretation of ECG in SNC80 and vehicle treated hearts.**

961

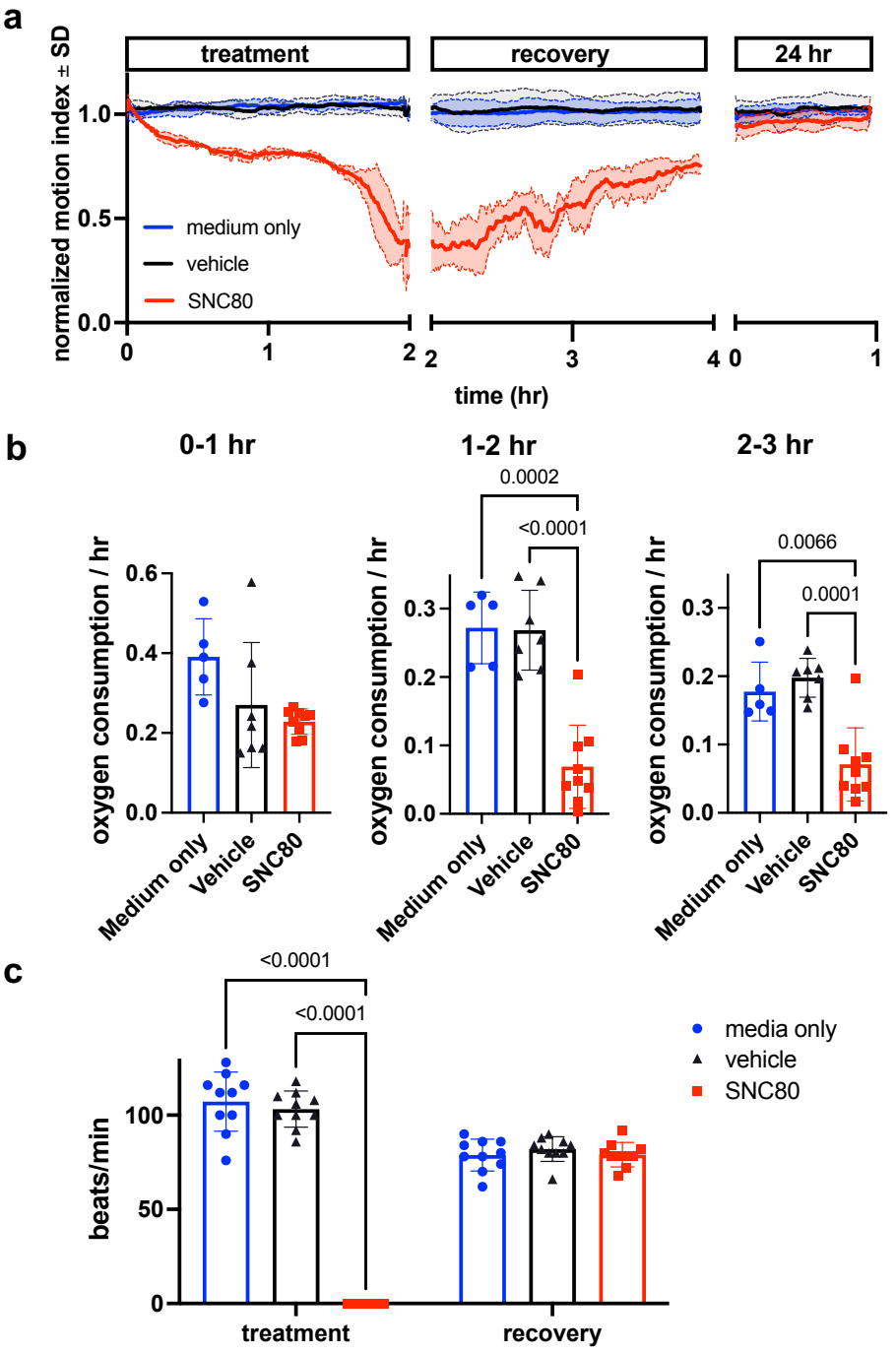

Figure 1

962

963

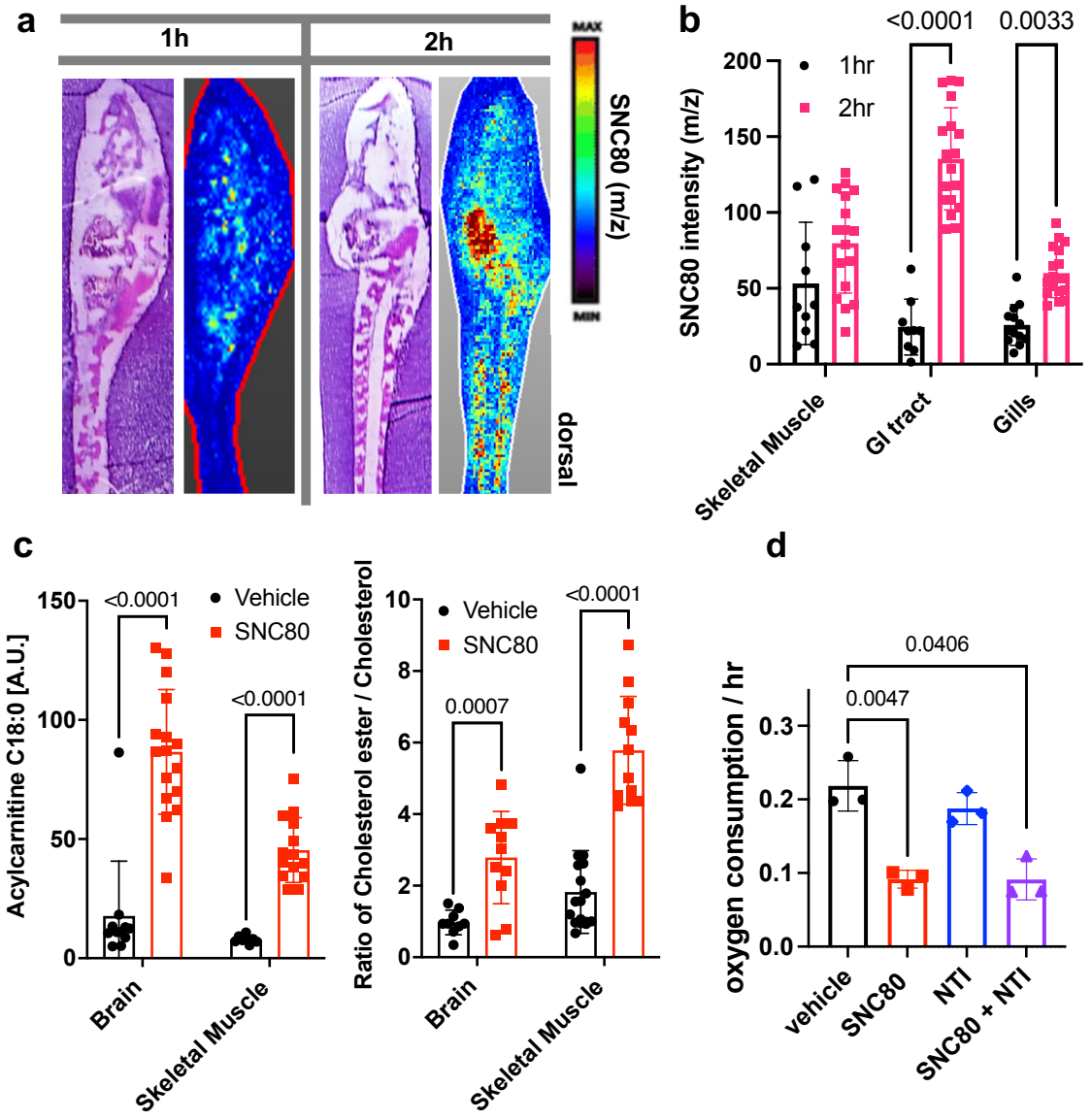

Figure 2

964

965

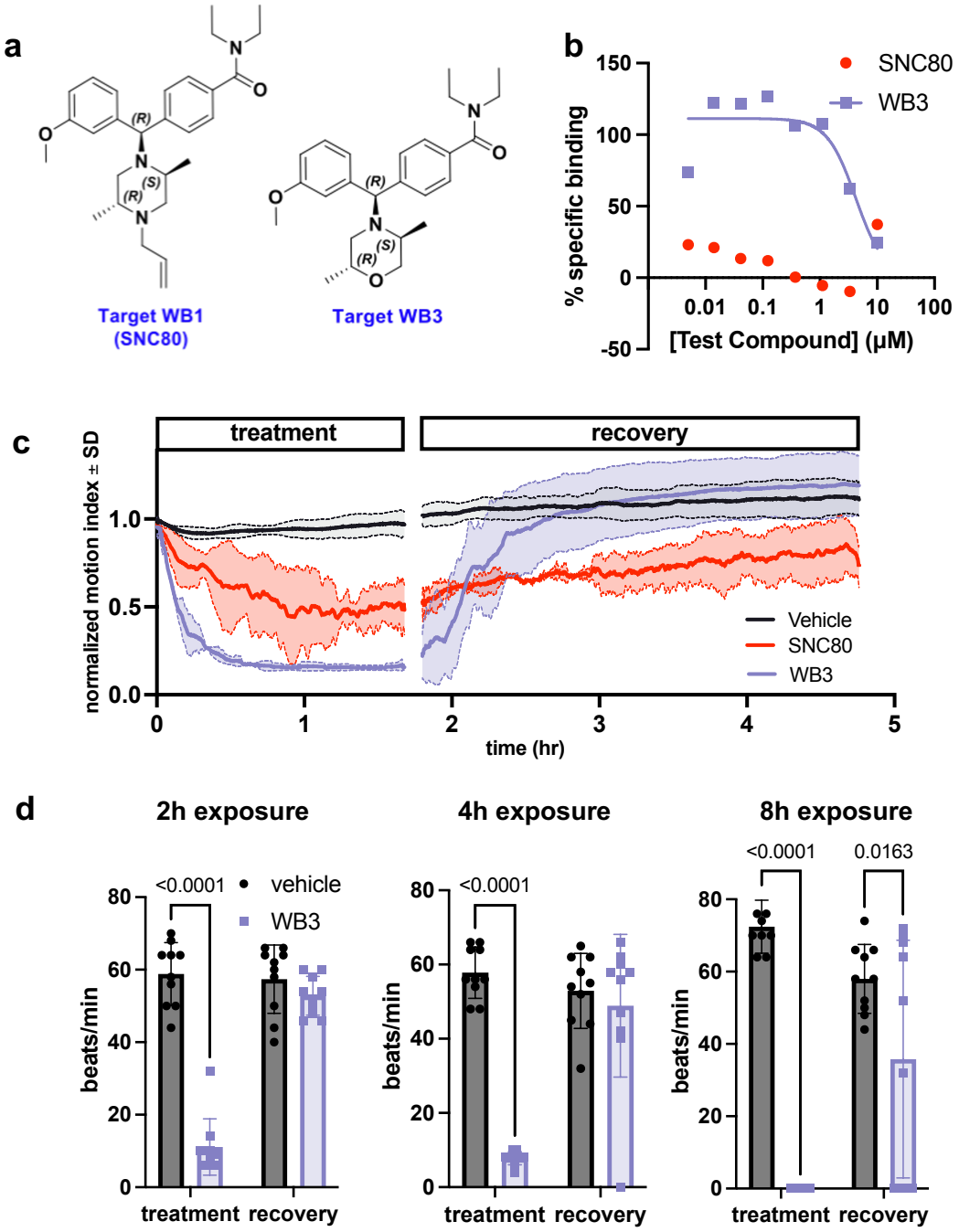

Figure 3

966

967

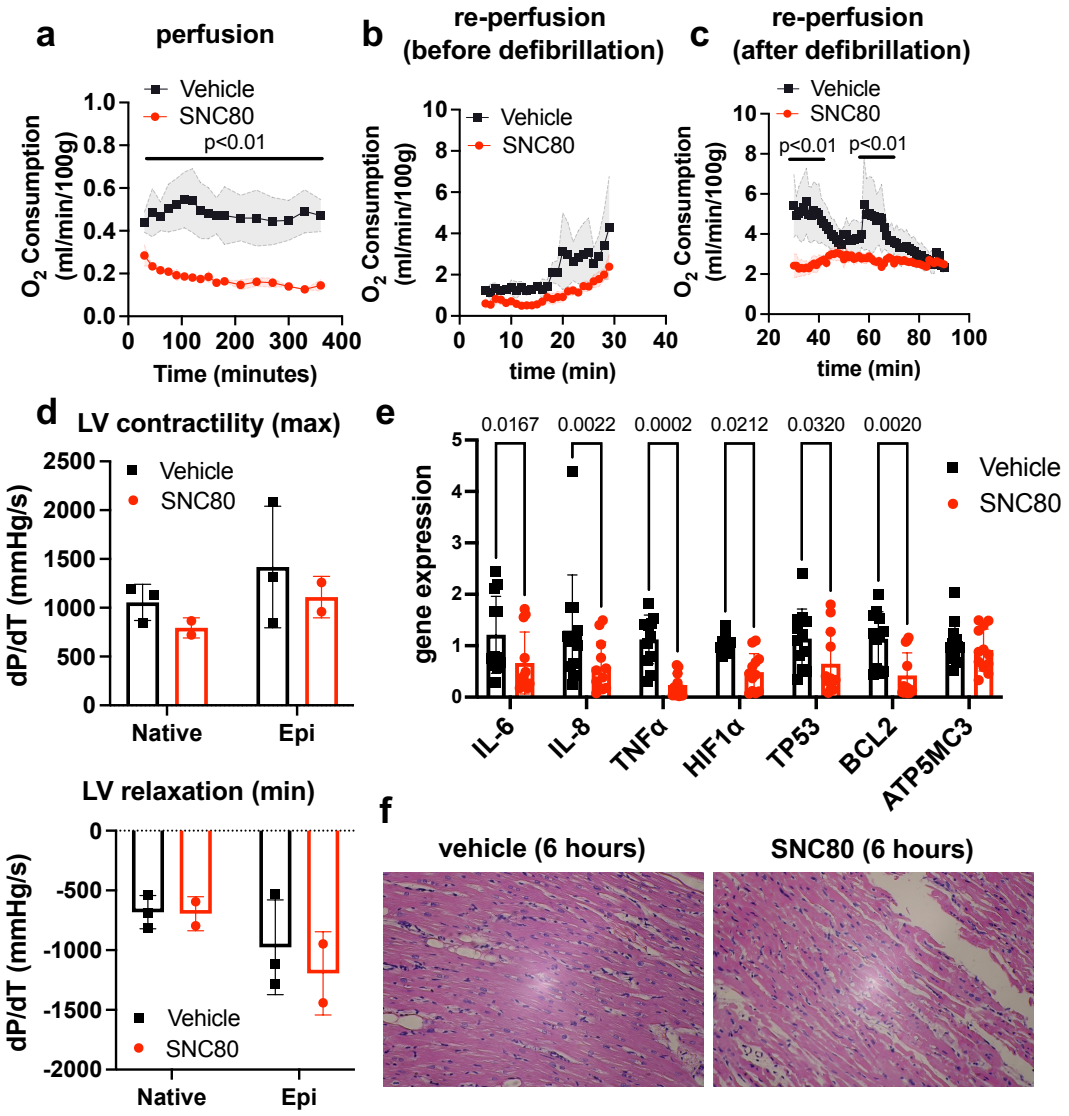

Figure 4

968

969

970

direct interaction	function	indirect interaction	function
CCBL1	• pyridoxal phosphate binding • cysteine-S-conjugate beta-lyase activity • L-glutamine aminotransferase activity • cellular modified amino acid metabolic process	ABCB1	• ABC-type bile acid transporter activity • regulation of fatty acid beta-oxidation • efflux transmembrane transporter activity
EAAT1	• L-glutamate transmembrane transporter activity	ACOX3	• fatty acid beta-oxidation using acyl-CoA oxidase • fatty acid binding
FUCA2	• alpha-L-fucosidase activity • glycoside catabolic process	CAMSAP2	• cytoplasmic microtubule organization • calmodulin binding
HM13	• peptidase activity • aspartic endopeptidase activity	COX6C	• mitochondrial electron transport, cytochrome c to oxygen • generation of precursor metabolites and energy
PTX3	• negative regulation of glycoprotein metabolic process • complement component C1q complex binding	ITGA7	• integrin-mediated signaling pathway • cell adhesion mediated by integrin
RPE65	• phosphatidylserine binding • retinoid metabolic process	NCX1	• calcium:sodium antiporter activity • calcium ion binding • regulation of the force of heart contraction
RPL27A	• structural constituent of ribosome cytoplasmic translation	ROBO1	• Roundabout signaling pathway • aorta development
RPL4	• structural constituent of ribosome cytoplasmic translation	RRP9	• RNA binding • rRNA processing
RPS25	• structural constituent of ribosome cytoplasmic translation		
TOMM40	• protein transmembrane transporter activity • protein targeting to mitochondrion • mitochondrial outer membrane translocase complex		
VMP1	• autophagosome membrane docking • plasma membrane phospholipid scrambling • lipoprotein transport		

Table 1

971

972

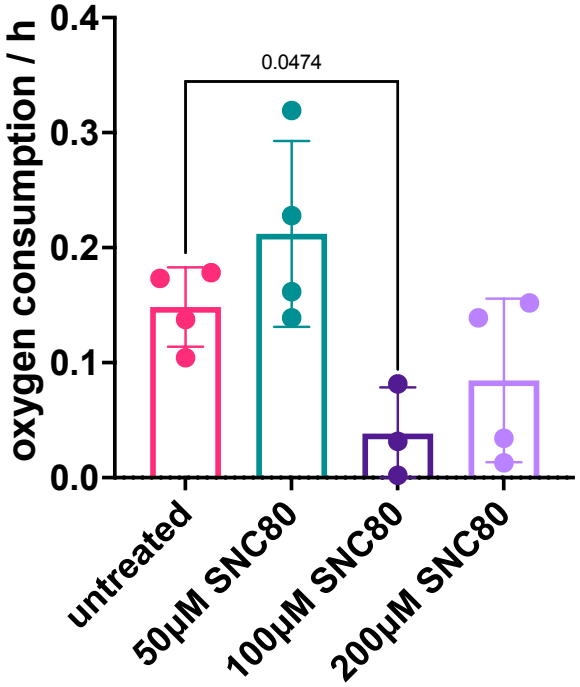

Supp. Figure S1

973
974

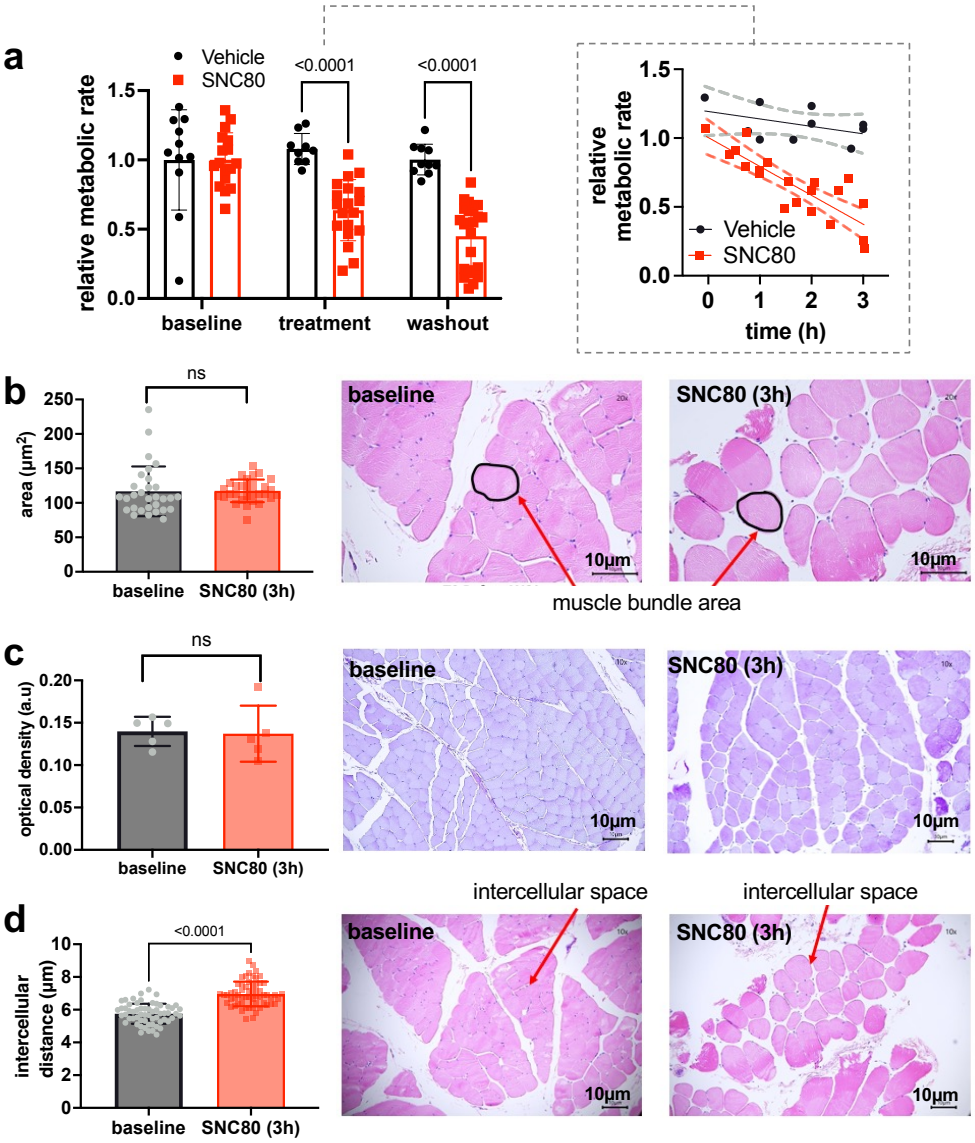

Supp. Figure S2

975

976

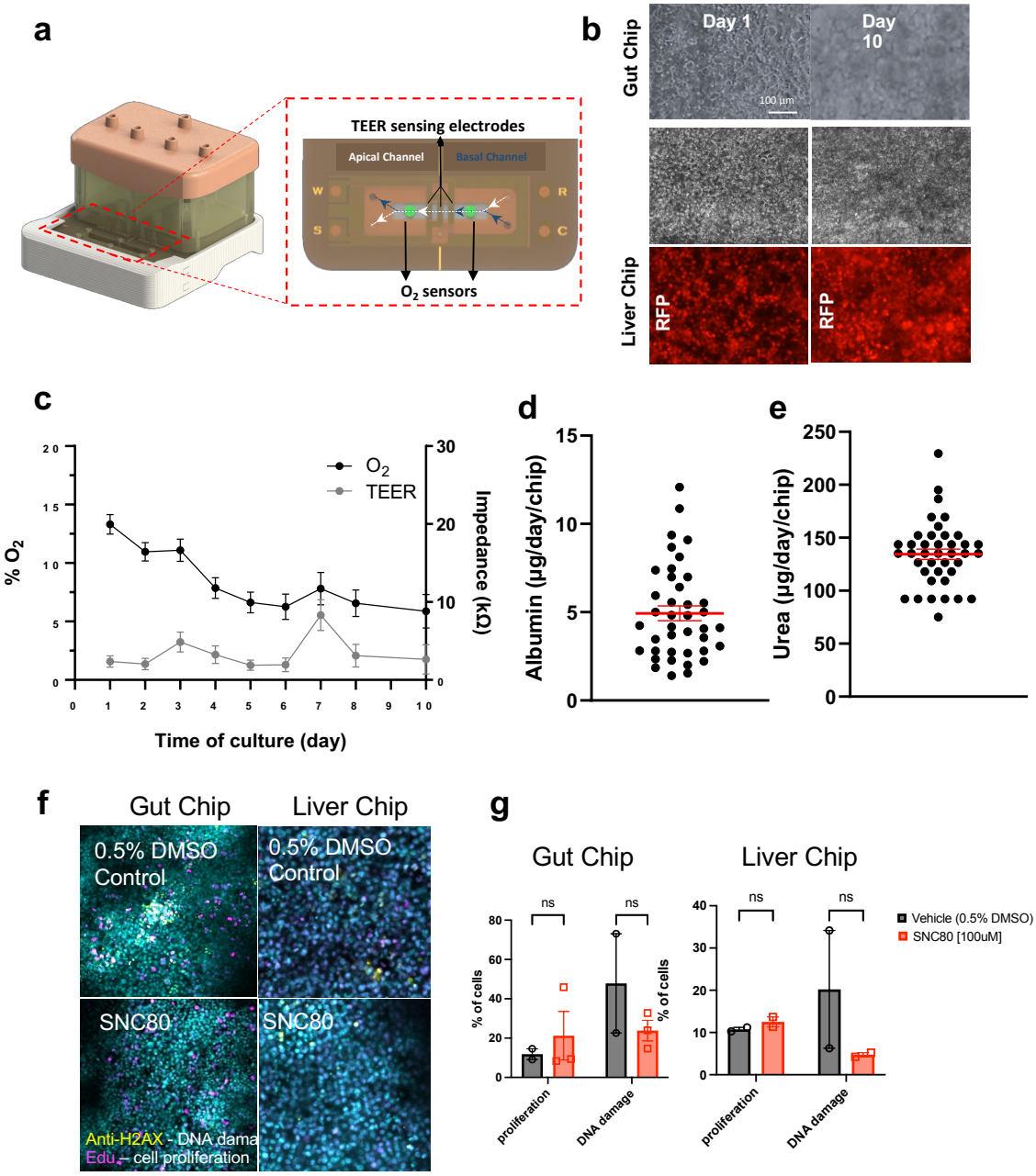

Supp. Figure S3

977

978

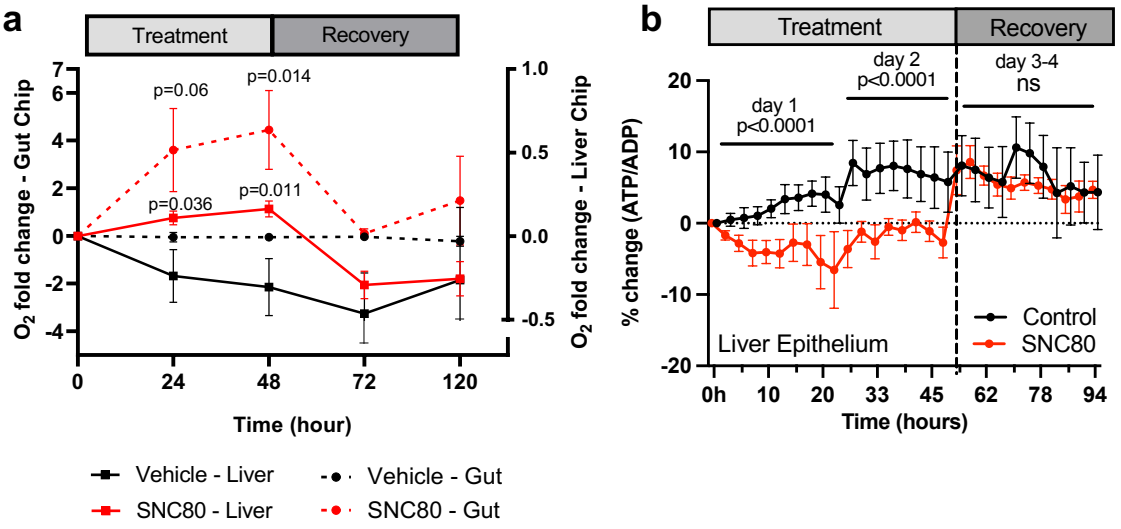

Supp. Figure S4

979

980

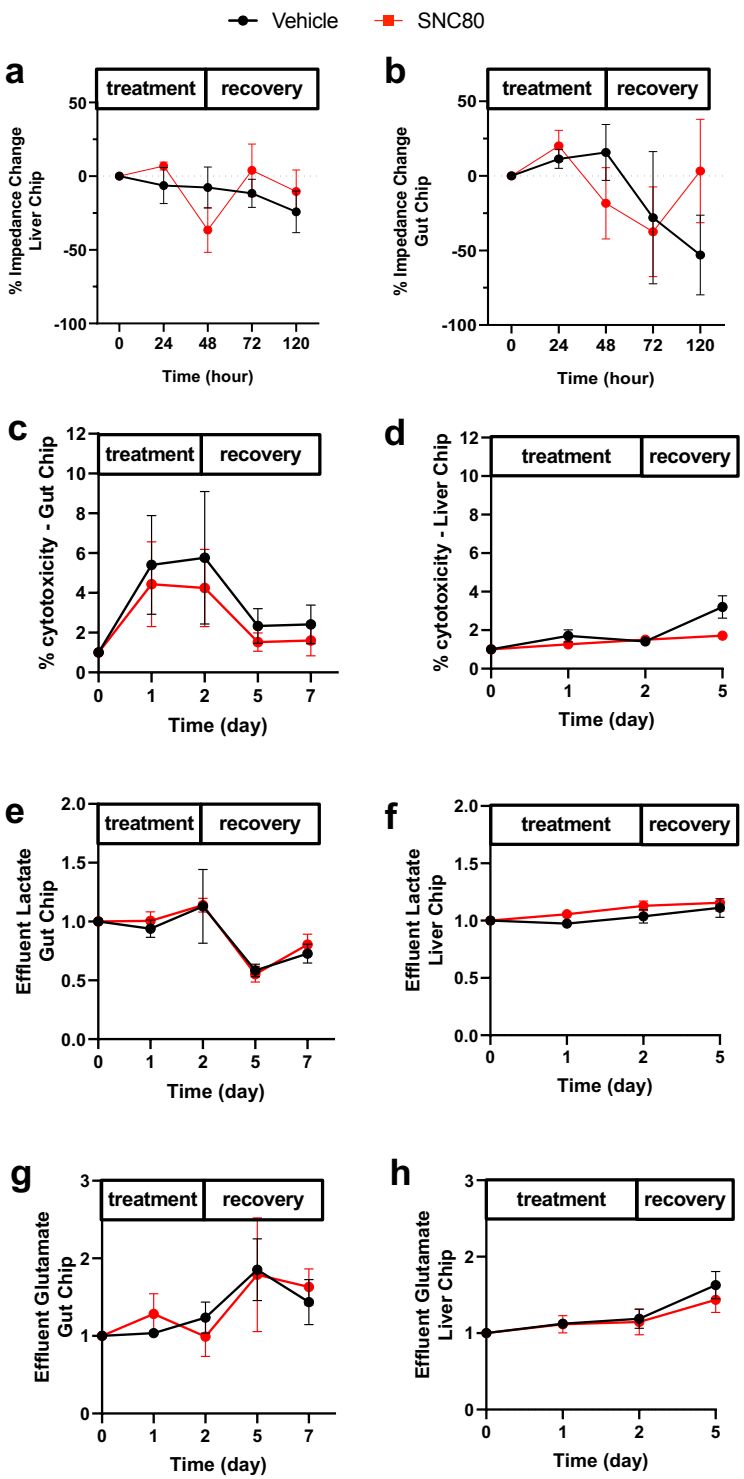

Supp. Figure S5

981

982

		Before recirculating					
		Pulse (bpm)	**Rate**	**Rhythm**	**P waves**	**QRS waves**	**T waves**
SNC80	P014	n/a	normocardic	irregular	no	no	n/a
	P015	n/a	tachycardic	irregular	no	no	n/a
	P019	n/a	n/a	n/a	n/a	n/a	n/a
	P023	12 bpm	bradycardic	irrregular	no	no	n/a
Vehicle	P016	n/a	tachycardic	irregular	no	no	n/a
	P020	n/a	tachycardic	irregular	no	no	n/a
	P024	n/a	tachycardia	irregular	no	no	n/a

		After defibrilation					
		Pulse (bpm)	**Rate**	**Rhythm**	**P waves**	**QRS waves**	**T waves**
SNC80	P014	132 bpm	tachycardic	regular	yes	yes	T wave elevation
	P015	96bpm	normocardic	irregular	yes	yes	Normal T waves
	P019	54 bpm	bradycardic	irregular	some	yes	Inconsistent T wave depression
	P023	96 bpm	normocardic	regular	no	no	Unable to assess (supraventricular tachycardia)
Vehicle	P016	144 bpm	tachycardic	regular	yes	yes	Slightly abnormal ST segment depression
	P020	132 bpm	tachycardic	regular	no	yes	T wave depression
	P024	138 bpm	tachycardic	regular	some	yes	T wave abnormal (P and T wave overlap)

Supp. Table S1

Supplemental Synthesis Description

<u>Step 1</u>: Synthesis of intermediate *N,N*-diethyl-4-formylbenzamide

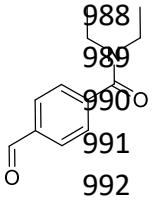

4-formylbenzoic acid (10 g, 66.61 mmol) and HATU (30.39 g, 79.93 mmol) were dissolved in DMF (500 mL) at 15 °C under N_2. The mixture was then warmed to 30 °C and stirred for 1 h. At this juncture, the mixture was cooled to 15 °C and DIEA (34.43 g, 266.43 mmol, 46.41 mL) and diethylamine (7.31 g, 99.91 mmol, 10.29 mL) were added dropwise together. The reaction was allowed to warm to rt and stirred for 12 h. The reaction mixture was diluted with H_2O (2000 mL), and then extracted with ethyl acetate (5000 mL x 3). The combined organic layers were washed with brine (1000 mL), dried over Na_2SO_4, filtered, and concentrated under reduced pressure to give a residue. The residue was purified by column chromatography (SiO_2, Petroleum ether/Ethyl acetate = 3/1 to 1/1) to give *N,N*-diethyl-4-formylbenzamide (57 g, 277.71 mmol, 83.38% yield) as a yellow solid. LC-MS m/z = 206.1 $[M+H]^+$.

<u>Step 2</u>: Synthesis of intermediate *N,N*-diethyl-4-[hydroxy(3-methoxyphenyl)methyl]benzamide

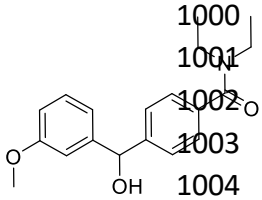

To a solution of *N,N*-diethyl-4-formylbenzamide (8 g, 38.98 mmol) in THF (320 mL) was dropwise added bromo-(3-methoxyphenyl)magnesium (1 M, 46.77 mL) at 0 °C under N_2. The reaction was stirred at 20 °C for 2 h, at which time it was diluted with H_2O (1000 mL), and then extracted with dichloromethane (500 mL x 3). The combined organic layers were washed with brine (300 mL), dried over Na_2SO_4, filtered, and concentrated under reduced pressure to give a residue. The residue was purified by column chromatography (SiO_2, Petroleum ether/Ethyl acetate = 3/1 to 1/1) to give *N,N*-diethyl-4-[hydroxy-(3-methoxyphenyl)methyl]benzamide (6 g, 19.15 mmol, 6.14% yield) as a white solid. LC-MS m/z = 314.1 $[M+H]^+$.

<u>Step 3:</u> Synthesis of intermediate 4-(chloro(3-methoxyphenyl)methyl)-*N,N*-diethylbenzamide

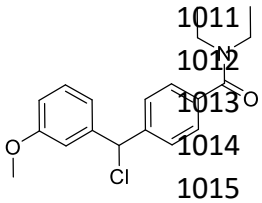

To a solution of *N,N*-diethyl-4-[hydroxy-(3-methoxyphenyl)methyl]benzamide (11.75 g, 37.49 mmol) in $CHCl_3$ (110 mL) was added dropwise HCl (12 M, 421.80 mL). The resulting mixture was stirred at 20 °C for 12 h, at which time it was diluted with H_2O (50 mL), and then extracted with dichloromethane (30 mL x 3). The combined organic layers were washed with brine (30 mL), dried over Na_2SO_4, filtered, and concentrated under reduced pressure to give 4-[chloro-(3-methoxyphenyl)methyl]-*N,N*-diethyl-benzamide (23 g, 69.31 mmol, 92.43% yield) as a yellow oil.

<u>Step 4:</u> Synthesis of WB3

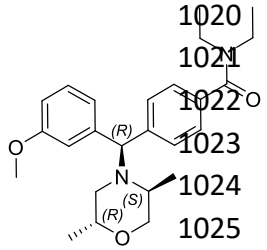

To a mixture of 4-[chloro-(3-methoxyphenyl)methyl]-*N,N*-diethyl-benzamide (23 g, 69.31 mmol) and (*2R,5S*)-2,5-dimethylmorpholine (15.97 g, 138.62 mmol) in ACN (230 mL) was added K_2CO_3 (19.16 g, 138.62 mmol). The resulting mixture was stirred at 80 °C for 4 days. The reaction mixture was filtered, and the mother liquor was directly concentrated. The residue was purified by column chromatography (SiO_2, Petroleum ether/Ethyl acetate = 5/1 to 2/1). The residue was further purified by preparative-HPLC (column: UniSil 10-120 C18 70x250mm; mobile phase: [water(FA)-ACN]; gradient:20%-50% B over 20 min) and the appropriate fractions were lyophilized. The residue was again further purified by preparative-HPLC (column: Phenomenex luna C18 (250*70mm,10 um); mobile phase: [water (FA)-ACN]; gradient:10%-50% B over 35 min) and the appropriate fractions were lyophilized to give WB3 (3.3 g, 8.03 mmol, 11.59% yield) as a white solid. LC-MS m/z = 296.1 $[M+H]^+$.

^{1}H NMR (400 MHz, $CDCl_3$) δ = 7.47 (d, J = 7.8 Hz, 2H), 7.34 - 7.27 (m, 3H), 6.88 (dd, *J* = 2.0, 8.3 Hz, 1H), 6.75 (d, *J* = 7.6 Hz, 1H), 6.72 - 6.67 (m, 1H), 5.32 (s, 1H), 3.81 (s, 3H), 3.76 - 3.66 (m, 2H), 3.64 - 3.45 (m, 2H), 3.44 - 3.24 (m, 3H), 2.61 (dd, *J* = 2.0, 11.6 Hz, 1H), 2.57 - 2.48 (m, 1H), 1.82 (dd, *J* = 9.5, 11.6 Hz, 1H), 1.24 (br d, *J* = 0.8 Hz, 3H), 1.12 (d, *J* = 6.1 Hz, 6H), 1.06 (d, *J* = 6.3 Hz, 3H).